UNIVERSITY OF UTRECHT

DEBYE INSTITUTE

NANOPHOTONICS GROUP

Size Analysis of Trapped Goldnanoparticles using Polarimetry

Author:
Anne de Beurs BSc

Supervisors:
M. Scholten MSc
Dr. J. Hernandez-Rueda
Dr. D. van Oosten

August 30, 2016

Abstract

We have developed a method of charging and trapping single gold spheres with a radius of 50 nm for the purpose of ablation. To achieve this we use electrospray ionisation to separate and trap these particles. Charged particles are trapped inside a linear ion trap. As we intend to do laser ablation on single gold nanospheres we need to determine whether the trapped particles are aggregated. Therefore, we test a method to do in-situ measurements of the size of the particles in the trap, by comparing the polarisation dependent scattering of those particles with Mie theory.

We have carried out experiments with a Helium-Neon laser and a 785 nm diode laser on five different particles for which the results seem to indicate radii of 466 ± 2 nm, 465 ± 1 nm, 577 ± 2 nm, 342 ± 1 nm and 577 ± 2 nm. A second experiment was done on different particles with three diode lasers (642 nm, 785 nm,852 nm) on two different particles. These experiments suggest particle sizes of 179 ± 1 nm and 179 ± 1 nm. As a single gold colloid has a radius of 50 nm, we found that trapped particles were aggregated.

Contents

1 Introduction

The Nanophotonics group investigates a number of different research subjects involving optics, ultra-cold atoms and the interaction of light and matter. One of the topics that is currently being investigated, is femtosecond laser ablation of different materials. In particular, surface ablation of dielectrics, semiconductors and metals have been carried out. See for instance the PhD thesis by H. Zhang [1] and master theses by J. Clarijs [2] and M. Scholten [3]. Besides ablation on homogeneous surfaces, the ablation process of droplets of gold nanoparticles on a semiconductor substrate has also been studied in the master thesis of G. Zomer [4].

1.1 Motivation

Laser ablation is any process where the irradiation of a surface with laser light results in removal of material. As the laser pulse duration is short with respect to the timescales of heat diffusion and structural changes in the lattice, femtosecond pulse lasers have a well localised energy deposition. Therefore its possible to remove material with sub-diffraction limit precision [5,6]. This makes them ideal for the manufacturing of nanoscale structures such as electronics or photonic devices [7,8]. High precision removal of material also has many applications in medicine. For example, the laser ablation process can be used for dentistry [9], for brain surgery [10] and refractive surgery [11]. During the process an extremely hot plasma is created, which can be used as energy efficient emitters of extreme ultra violet and x-ray light [12,13]. Femtosecond laser ablation has also been an active field of research [14, 15]. One of the difficulties encountered in describing femtosecond laser ablation experiments is that simulations based on the theory take considerable computational time. To accurately describe the energy deposition of a femtosecond laser pulse many different processes need to be taken into account, some of which are non-linear. These mechanisms describe the way the laser modifies the dielectric function of the excited material both in time and in space. Reducing the dimensionality of the problem would greatly simplify the theoretical description and reduce computational difficulties. Therefore, we intend to ablate trapped single gold colloids[1], where their properties can be considered spatially homogeneous.

[1] Colloids are composite particles dispersed in a substance that are large enough to be seen by an optical microscope, but small enough to experience Brownian motion under the influence of random collisions with the surrounding medium. These random movements were discovered by Robbert Brown [16] and later explained by Albert Einstein [17].

1.2 Summary

To achieve the goal of ablating single colloids, we first need to separate and trap single gold nanospheres. For this purpose we used electrospray ionisation to inject the particles into a linear ion trap. During this process particles are charged and separated through a series of Coulomb explosions. Electrospray has been studied for over a century [18]. Usually electrospray is done in a regime where droplets ejected out of a capillary deform into a 98.6°cone that is called a Taylor cone [19]. From this cone fluid is ejected through a jet and is then nebulised as the fluid phase that carries the charged particles evaporates. Electrospray has been used as a method for a number of different applications. It is used in mass spectrometry [20], depositing thin films [21,22] and even as thrusters for spacecraft propulsion [23].

We trap the particles using an quadrupole ion trap, pioneered by Wolfgang Paul [24] for which he received a Nobel price in 1989 [25]. Electric quadrupole traps are a frequently used tool in the field of mass spectrometry [26,27]. The parameters that determine the stability of charged particles inside the trap are proportional to the charge-to-mass ratio. Therefore this ratio can be found by determining the edge of the stability region.

However because colloidal particles tend aggregate, a way to distinguish between a single colloid and an aggregate of many colloids is needed. For this purpose we presented a method to do in-situ measurements of the size of the particles in the trap. We have measured the polarisation dependence of the scattering intensity of gold nanoparticles inside the trap and compared these experimental results with numerical Mie Theory calculations, from which we can retrieve the radius of these spheres. Mie theory is an exact solution for the Maxwell's equation, for scattering on homogeneous spheres. It is named after Gustaph Mie who published the solution in 1908 [28], although it is unlikely that he was the first to find the solution. Mie theory is used in a number of different fields to determine the size of colloidal particles, from bloodcells [29] to Aerosols [30].

1.3 Outline

The theory behind the trapping and electrospray setup will be discussed in section 2, In section 3 we will discuss the experimental methods for electrospraying and trapping the nano particles will be discussed. Then in section 4, the Mie scattering theory will be explained. In section 5 the setup for the polarimetry experiments will be covered. In section 6 we will show the results of the experiments. In section 7 these results will be discussed and a conclusion will be drawn and in section 8, we will give an outlook on our goals and how we can improve our methods.

Part I

Preparing the Particles in the Trap

2 Theory

2.1 Trapping Ions in a Time-Oscillating Electric Field

To isolate charged gold nanospheres a trapping method is required. We need a method that works in vacuum therefore, we will use an electric field. Earnshaw's theory states that it is impossible to trap point charges in a vacuum with a static electric field [31]. As the divergence of the electric field is zero in free space, the potential cannot have local minima. However it is possible to trap particles by using a combination of electric and magnetic fields. This is done in Penning traps [32]. It is also possible to use a combination of electric and centrifugal forces. This is applied in Kingdon traps [33] and Orbi traps [34]. We chose to use a method based on a time-oscillating quadrupole field, a trap also known as a Paul trap [25]. In Cartesian coordinates of a perfect quadrupole can be written in the form [25]

$$\phi = \frac{\phi_0}{2r_0^2}(\alpha x^2 + \beta y^2 + \gamma z^2), \tag{2.1}$$

where ϕ_0 is the potential at the trap axis, r_0 is the distance between the rod surface and the trap axis and α, β and γ are dimensionless coefficients that depend on the geometry of the trap. Traditionally 3-D Paul traps have been used in mass spectrometry, however we will use a 2-D Linear Ion Trap (LIT) [35]. The linear ion trap offers a number of advantages over a three dimensional design: The absence of a quadrupole field on one of the axis increases the fraction of charged particles that will penetrate into the trap [35]. Because the potential is independent on the length of the rods, it is possible to have much larger trapping volume [36]. By contrast increasing the volume of the 3D designs also increases the distance of the electrodes to the center of the trap, increasing the potential needed to trap particles.

In practice a 2D field is achieved by using four long parallel rods, this geometry can be seen in Fig 2.1a. Here the long axis component of the field will be zero in the trap due to the symmetry of the system.

$$\phi = \frac{\phi_0}{2r_0^2}(\alpha x^2 + \beta y^2). \tag{2.2}$$

This solution needs to satisfy the Laplace equation $\nabla^2\Phi = 0$ so $\alpha = -\beta$. As ϕ_0 is the potential difference between the x-rods and the y-rods, we get the boundary

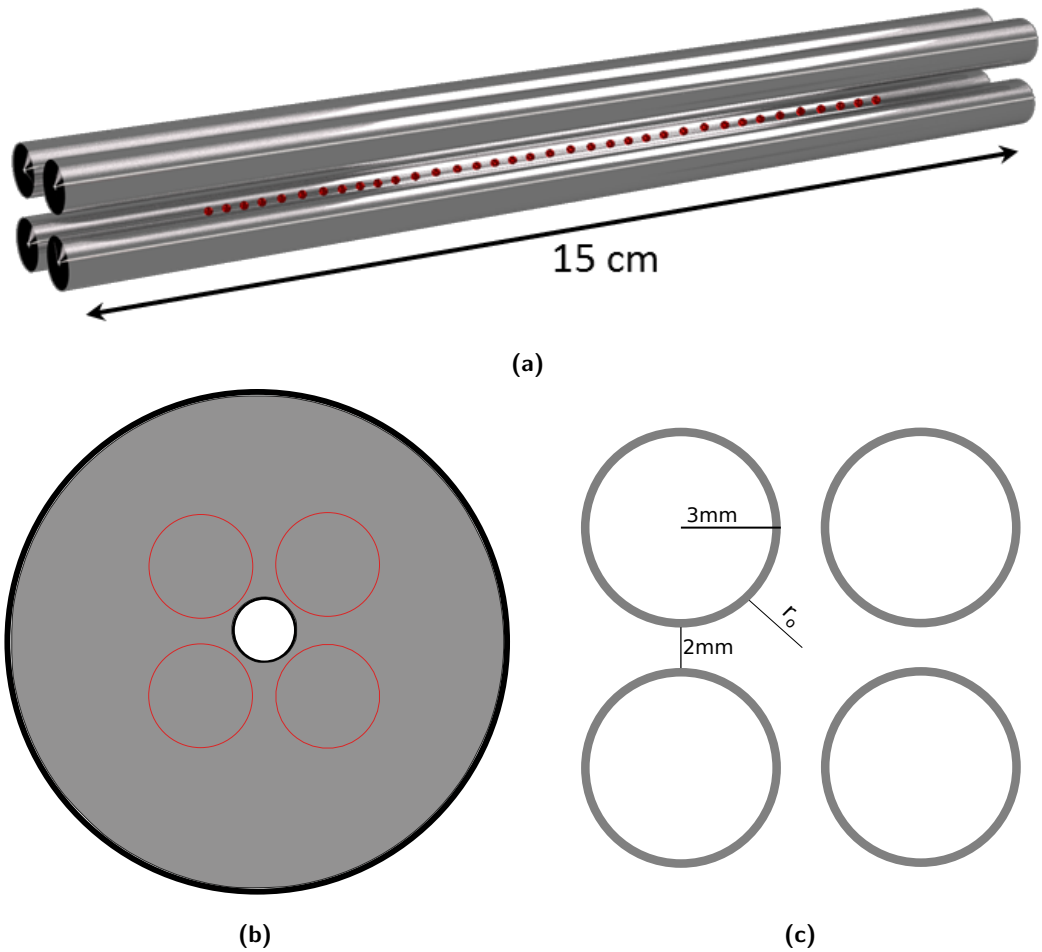

Figure 2.1: Geometry of the trap. **a**) shows a schematic overview of the rods. **b**) shows the frontview of the trap, a ground plate with a small hole in the middle that serves both as a entry point for gold colloids and to allow optical access for the probe laser. The red circles show where the rods are attached. **c**) shows a cross section of the rods and the scale of the rods.

condition.

$$\frac{\alpha\phi_0 + \alpha\phi_0}{2} = \phi_0, \tag{2.3}$$

from which we get $\alpha = 1$. This leads us to the following potential,

$$\phi = \frac{\phi_0}{2r_0^2}(x^2 - y^2). \tag{2.4}$$

A perfect electric quadrupole field is created by using hyperbolic rods. However cylindrical rods are often preferred over hyperbolic designs, due to the lower cost and higher speed of fabrication. The field of a long cylinder has higher order terms in the multipole expansion. Still its possible to suppress the higher order terms in the expansion, by carefully choosing the right geometry. According to Denison [37] and Gibson [38] it is possible to approximate the field of the hyperbolic rods with cylindrical rods by choosing $r \approx 1.13\ r_0$ where r is the radius of the rods. In our setup $r_0 = 2.66\,\text{mm}$ and $r = 3\,\text{mm}$ (see Fig. 2.1c). Equation 2.4 corresponds to a saddle point, which is only stable in one dimension, however by choosing ϕ_0 to be sinusoidal in time (see Eq. 2.5) a stable solution is possible due to a small residual force, similar to how a small sphere can be stable on a rotating saddle,

$$\phi_0(t) = U + V\cos(\Omega t), \tag{2.5}$$

where U is a constant potential, V is the amplitude of a oscillating potential and Ω is the frequency of V. Considering the equation of motion in the one dimension

$$F_x(t) = -Q\,\frac{\mathrm{d}\phi}{\mathrm{d}x} + F_{\text{friction}} = -Q\,[U + V\cos(\Omega t)]\,\frac{x}{r_0^2} - b\,\frac{\mathrm{d}x}{\mathrm{d}t}. \tag{2.6}$$

Where F_{friction} is the frictional force and b is the linear drag constant. We will assume Stokes drag $b = 6\pi\eta r_{\text{particle}}$ for atmospheric conditions. Here η is the dynamic viscosity and r_{particle} is the radius of a particle. At lower pressures, the free path length λ_{fp} gets large compared to the size of the particles and the no-slip condition that is assumed for the derivation of Stokes law is no longer valid. In this case we use the Cunningham's correction factor (seen in Eq. 2.7 [39]) to divide the friction to compensate for slipping,

$$b = \frac{6\pi\eta}{r_{\text{particle}}}(1 + 2\,\text{Kn}[\text{A}_1 + \text{A}_2\text{e}^{-\frac{\text{A}_3}{\text{Kn}}}]),. \tag{2.7}$$

Where $\text{Kn} = \frac{\lambda_{\text{fp}}}{r_{\text{particle}}}$ is the Knudsen number and A_1, A_2 and A_3 are dimensionless coefficients dependent on the medium. If the terms in Eq 2.6 are reordered, we get the following equation

$$m\,\frac{\mathrm{d}^2x}{\mathrm{d}t^2} + Q[U + V\cos(\Omega t)]\,\frac{x}{r_0^2} - \text{b}\,\frac{\mathrm{d}x}{\mathrm{d}t} = 0. \tag{2.8}$$

It is possible to rewrite equation 2.8 in terms of dimensionless parameters,

$$\frac{\mathrm{d}^2x}{\mathrm{d}\tau^2} + (a - 2q\cos(2\tau)x + 2\kappa\frac{\mathrm{d}x}{\mathrm{d}\tau} = 0, \tag{2.9}$$

where $\tau = \frac{\Omega}{2}t$ is a dimensionless time, $a = \frac{4QU}{m\Omega^2 r_0^2}$ is a dimensionless parameter that indicates the influence of the time-independent component of the field on the particle, $q = -\frac{2QV}{m\Omega^2 r_o^2}$ is a dimensionless parameter that indicates the influence of the time dependent component of the field field on the particle and $\kappa = -\frac{b}{2m\Omega}$ is the dimensionless friction parameter. For $\kappa = 0$ this has the form of the well studied Mathieu equation [40]. By trying a solution of the form [41]

$$x = w(\tau)e^{-\kappa\tau}, \tag{2.10}$$

we get the following equation for $w(\tau)$,

$$\frac{\mathrm{d}^2w(\tau)}{\mathrm{d}\tau^2} + (a - \kappa^2 - 2q\cos(2\tau))w(\tau) = 0, \tag{2.11}$$

which is in the form of the Mathieu equation in w. This will generate solutions of the form [41],

$$w(\tau) = \phi(\tau)A\mathrm{e}^{\mathrm{i}\alpha\tau+\beta\tau} + \phi(-\tau)B\mathrm{e}^{-\mathrm{i}\alpha\tau-\beta\tau}. \tag{2.12}$$

Where $\phi(\tau)$ is periodical with the field. For any stable solution, the real part of $x(\tau)$ has to decrease in time which means that $\kappa < \beta$. Figure 2.2 illustrates the stability region as a function of parameters a and q in atmospheric pressure and vacuum respectively. The lines indicate the edges of stability on the x-axis and the y-axis and the yellow area indicates the parameters for which the system is stable on both axes. We have chosen not to use a constant potential term so that $a = 0$, because the region of stability is the largest without a D.C. potential term. In vacuum the stability condition is then given by:

$$\left|q\right| = -\frac{2QV}{m\Omega^2 r_o^2} \leq 0.92 \tag{2.13}$$

Particles inside the trap will oscillate with a fast micro motion with the frequency of the trap superimposed on a lower frequency secular motion [41]. Without damping and assuming $\left|q\right| \ll 1$ the equation of motion can be described by [42]

$$u_t = u_0(1 - \frac{q}{2}\cos(\Omega t))cos(\omega_{\mathrm{sec}}t), \tag{2.14}$$

where $\omega_{\mathrm{sec}} = \frac{\sqrt{q^2/2}}{2}\Omega$ is the secular frequency. Assuming q is sufficiently small large scale motions are driven by the secular motion. Describing the secular motion as a

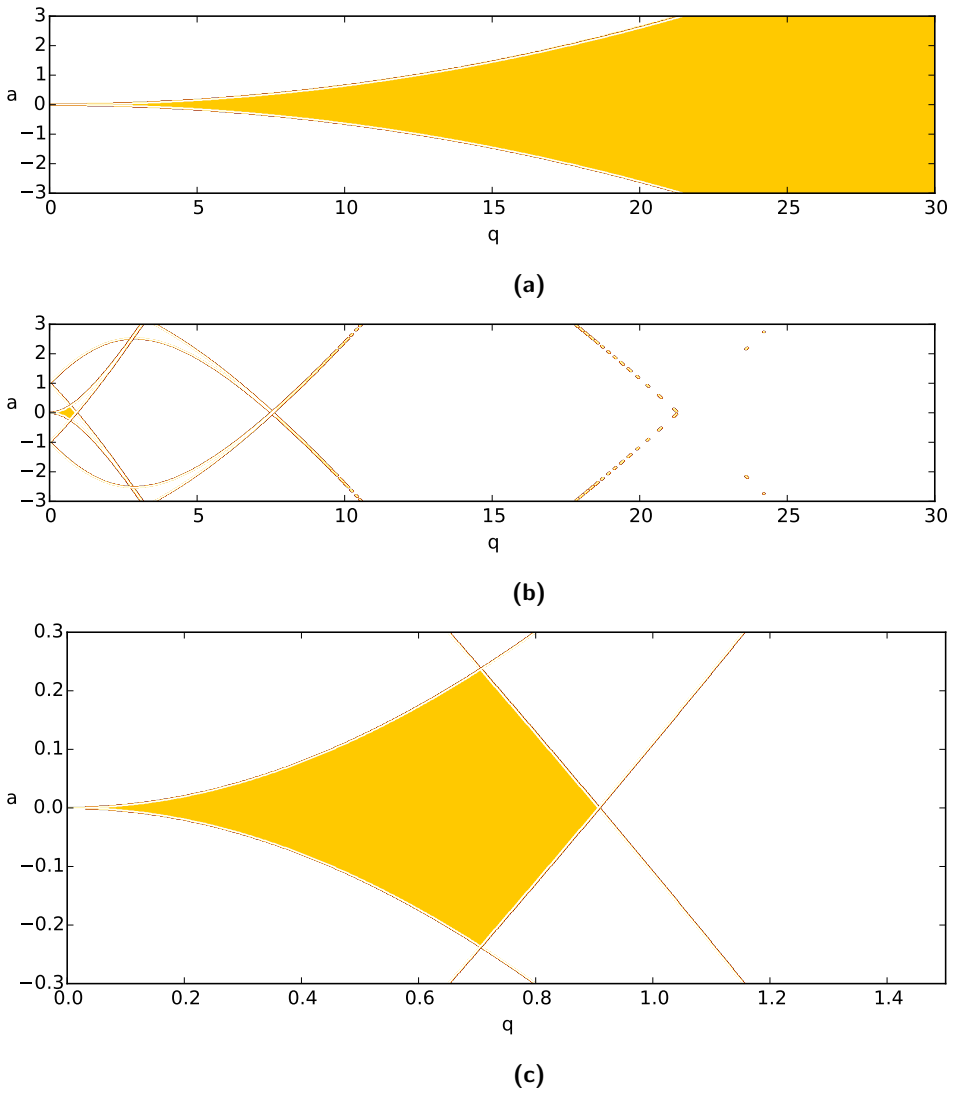

Figure 2.2: stability regions of the trap under different circumstances, the edge of stability on both the x and y axes is denoted by lines, the coloured area's signify that a particle is stable on both axes with these parameters, **a**) shows the stability zone at atmospheric pressure. **b**) shows the stability zone at 20 Pa, this is a typical pressure after evacuating the chamber. **c**) shows a close-up of the relevant region of **b**) These graphs are based on numerical calculations.

motion inside a harmonic potential gives a rough estimate of the energy needed to pull a particle out of the trap.

$$\begin{aligned} V_{depth} &= \frac{1}{2} m\omega_r^2 r_0^2, \\ V_{depth} &= \Omega^2 \frac{1}{16} m r_0^2 q^2. \end{aligned} \tag{2.15}$$

Filling in the expression for q in Eq. 2.15,

$$V_{depth} = \frac{1}{4}\frac{Q^2V^2}{m\Omega^2 r_o^2} = \frac{1}{8}qQV. \tag{2.16}$$

As the trap selects charge to mass ratios this means that it takes more effort to push large aggregates out of the trap when friction is neglectible then single nanoparticles.

2.2 Electrospray Ionization

We use electrospray ionization as a method to isolate the gold nanoparticles. In this process a high voltage is applied between the conductive layer of a capillary and a ground plate. When a liquid medium containing an analyte is ejected from the capillary, both the medium and the analyte will be ionised by the field. Usually electrospray ionisation is used near the conditions where a Taylor cone forms at the capillary. A droplet at the end of the capillary is deformed as the electric field increases until a equilibrium cone with 49.3°semi-vertical angle forms at the end of the capillary. Increasing the field strength further will cause a jet to appear at the end of the cone emitting fluid towards the electrode. As the liquid medium in this jet evaporates, the charge density increases until the outward pressure of the electric force will overcome the surface tension in a Coulomb explosion [43]. During a Coulomb explosion ions and smaller charged droplets are ejected untill the charge density is sufficiently reduced for the droplet to become stable again. As these smaller droplets travel through air and more of the liquid medium start to evaporate this process repeats itself repeatedly until a nebula of charged particles has formed. The maximum charge density a droplet may contain before it becomes unstable has been derived for spherical droplets by Lord Rayleigh [44], a spherical droplet can only be stable if $Q < Q_r$, where

$$Q_r = (8\pi\gamma\epsilon_0 D^3)^{\frac{1}{2}}. \tag{2.17}$$

The process is illustrated in Fig. 2.3.

Taylor cones were first explained by Sir Geoffrey Taylor in 1963 [19]. He derived the characteristics of these cones by calculating if a cone could be in equilibrium with the surface tension under the assumption that the surface of the cone is at equipotential as the fluid is conducting. He determined that the field for which the surface tension and electrical potential are in equilibrium in a cone has to be

$$V_{cone} = V_0 + AR^{\frac{1}{2}}\mathrm{P}_{\frac{1}{2}}(\theta), \tag{2.18}$$

where R is the radial coordinate, $P_{\frac{1}{2}}(\theta)$ is the half-order Legendre function (see equation A.8). For a cone to be at a constant potential, the Legendre term has to be 0,

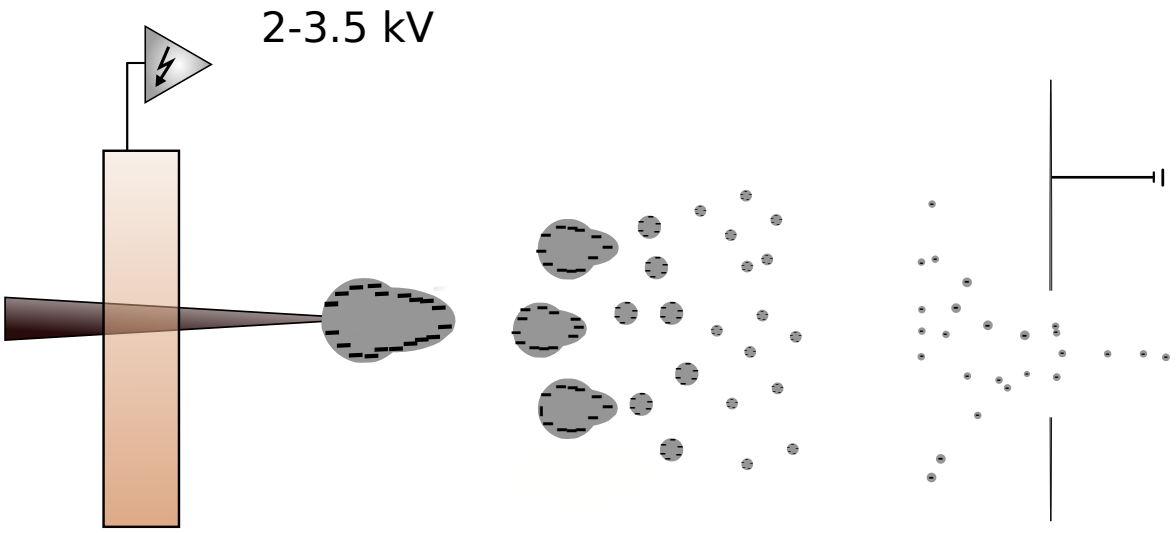

Figure 2.3: Schematic image of the electrospray process.

which is only true for $\theta_0 = 130°$, this angle corresponds to a semi-vertical angle of $\pi - \theta_0 = 49.3°$.

3 Experimental Setup

3.1 Electrospray Method

Gold nanospheres surface-coated with Polyvinylpyrrolidone (PVP) suspended in water with a concentration of $0.05\,\mathrm{g\,L^{-1}}$ were acquired [45]. The PVP surface coating helps to prevent aggregation of the colloids through steric repulsion. Compared to other stabilisers PVP has the advantages of binding strongly to metallic surfaces, and particles with a PVP coating can be stable in a wide variety of solvents. This suspension is diluted with ethanol in a ratio of 9:1. Ethanol is chosen as a solvent for its low surface tension, easing the criterion for instability (see equation 2.17) and because ethanol evaporates rapidly. These properties of ethanol increase the rate of coulomb explosions, and thus the rate of separation of the charged particles. The setup used is shown in Fig. 3.1. We used 1cc syringes with an inner diameter (ID) of 4.8mm, we attached a 0.22 µm filter to remove large aggregates formed in the dispersion. The syringes where placed in a syringe pump, which kept the volumetric flow rate constant at $40\,\mathrm{\mu L\,h^{-1}}$.

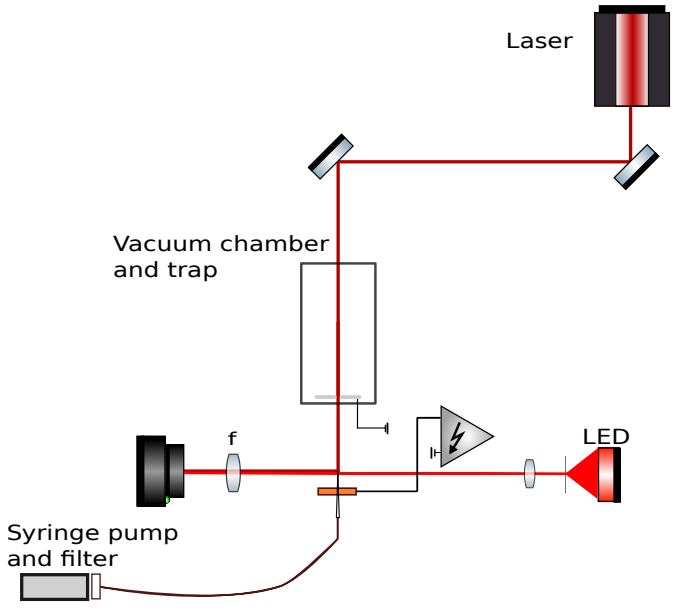

Figure 3.1: Image setup for electrospray, f2= 50 mm

The fluid then flows through a 30 cm long fused silica tube with a ID of 100 µm. This tube is connected to a fused silica emitter tip (15 µm ID). As discussed in Sec. 2.2 we suspect the Taylor Cone could be a cause of aggregation, to reduce the size of a possible Taylor cone the ID of the emitter is chosen to be smaller then the size of the jet coming from the Taylor Cone that was observed in earlier experiments [46] that used a 200 µm ID tip. The tip is fastened to a brass electrode which is connected to a high voltage power supply. Which is set to give a potential difference of around 2.5 kV between the tip and the grounded plate on the side of the trap (over 1.5 cm), after the dispersion is pumped through the tip, the gold particles are sprayed through the electrospray process described in section 2.2.

(a)

(b)

Figure 3.2: Images of the electrospray and the emitter all at 2.2kV, **a**) shows a picture of the LED light, at 2 kV between the tip and the ground plate, **b**) shows an picture where the ejection is mostly in a jet mode, at 1.8 kV between the tip and the ground plate, **c**) shows a picture where a very homogeneous spray is emitted from the tip, at 3 kV between the tip and the ground plate.

An imaging setup was used (see 3.1) to get a better understanding of the process and get a sense of the size of a possible Taylor cone. The spray was illuminated by a

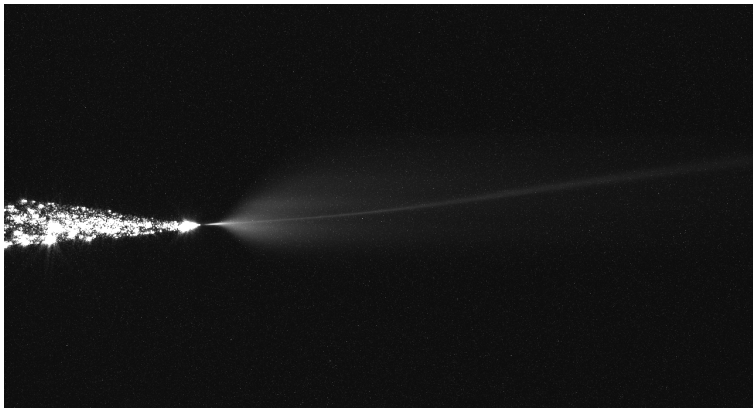

(a)

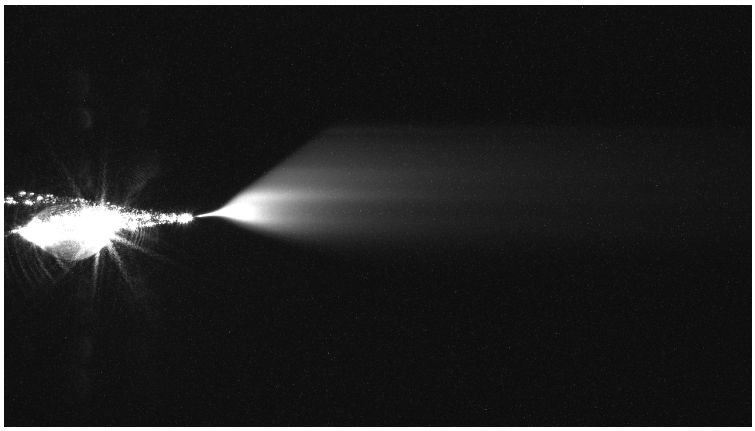

(b)

Figure 3.3: Images of the electrospray and the emitter at different potentials, **a**) shows an picture where the ejection is mostly in a jet mode, at $1.8\,\mathrm{kV}$ between the tip and the ground plate, **b**) shows a picture where a very homogeneous spray is emitted from the tip, at $3\,\mathrm{kV}$ between the tip and the ground plate.

Helium Neon laser (632 nm,2 mW) aligned through the hole in the grounded plate onto the emitter tip, the light scattered from te spray is collected on the camera. In addition a light emitting diode was used to create a high resolution shadow graph of the emitter. Imaging the electrospray with just the LED proved to be difficult due to the high degree of transparency of the diluted electrospray. Many attempts at creating electrospray experienced frequent clogging of the silica tubes, causing inconsistent flow. This is likely due to the properties of the PVP coating as it is sometimes used to attach gold to silicon surfaces [47]. In Fig. 3.2-3.3 a few pictures of the spray are shown under different circumstances, the Taylor cone is not observable in these pictures, so it is either not present or very small and is therefore unlikely to be a major cause of aggregation.

3.2 Paul trap and vacuum chamber

The quadruple ion trap (shown in Fig. 2.1a) consists of four 15 cm long stainless steel cylindrical rods attached to two Polyoxymethylene endcaps, on one of these endcaps a grounded metal plate was attached as can be seen in Fig. 3.4 Both end-

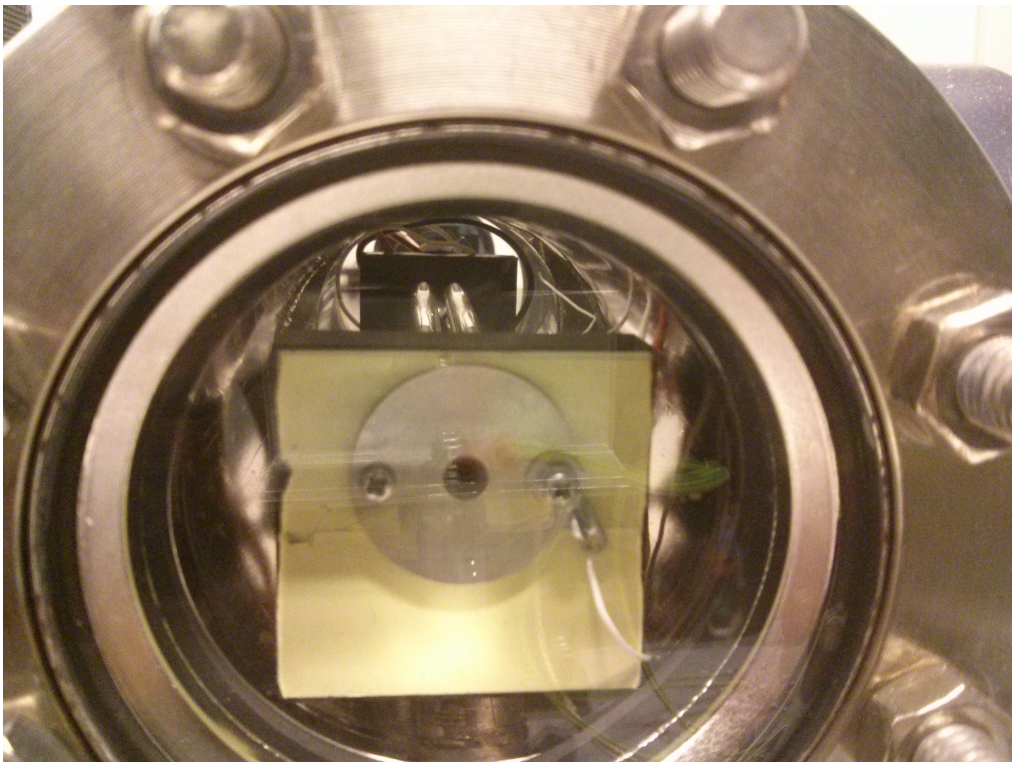

Figure 3.4: Frontside of the trap as placed in the vacuum chamber

caps have a 1 mm hole on the trap axis for optical access that also serves as a entry point for the particles as described in 3.1. The trap is placed in the vacuum chamber as can be seen in Fig.3.4. The two rods on the x-axis were connected with a high voltage A.C. power source that was controlled by a function generator, while the 2 rods on the y-axis were grounded. As the stability parameter q scales with U/Ω^2, a broad choice in trapping parameters is possible. We found however that more particles stayed trapped at high values for both U and Ω, possibly because the trap depth Eq. 2.16) scales with $Q\,U$, making it more difficult to perturb the particles out of the trap. Typically the trapping potential was set at about 600 V. At higher trapping potentials corona discharge would occur when evacuating the vacuum chamber. Up

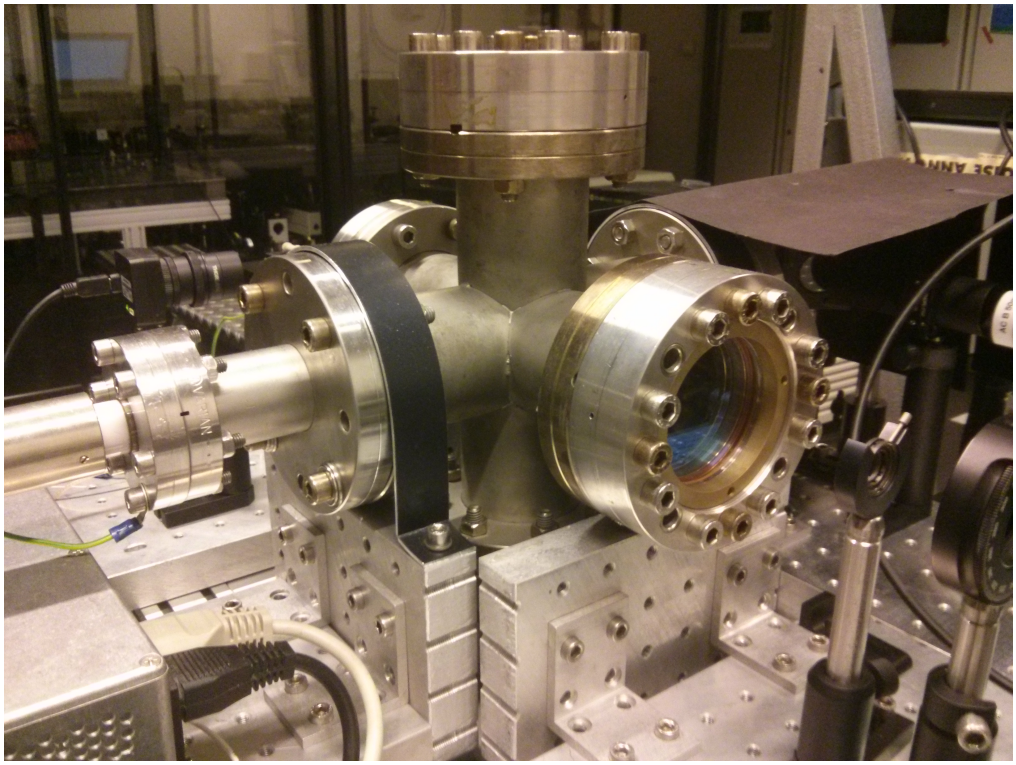

Figure 3.5: Overview of the vacuum chamber

to roughly 60 particles could be simultaneously trapped. After trapping a sufficient amount of particles the chamber was evacuated to a pressure of about 20 Pa. Some experiments were done at atmospheric pressure but in possible future ablation experiments it is important to be able to reliably predict the trajectory of the particles and as such would want to remove thermal motion of the particles. If the chamber gets evacuated too quickly, particles are pulled out of the trap by air flow. This should be avoided as this process is likely to select high mass aggregates. Larger particles have a larger trap depth Eq. 2.15.

Part II

Measuring the Size of the Gold Nanoparticles

4 Mie Theory

To calculate the size of the particles based on scattering measurements we need to know how results from scattering experiments on a particle relate to the size of that particle. For that reason, we use Mie theory calculations. The Mie solution for the Maxwells equations describes scattering of light on homogeneous spheres in the absence of surface charges or currents. Although aggregated particles may well be non-spherical, Mie theory can still be a reasonable first order approximation. A summary of the derivation based on Bohren and Huffmann [48] as well as a discussion of relevant parameters for determining the particle size will follow.

Assuming no free charges Maxwell's equations of time-harmonic electro-magnetic field in a homogeneous linear medium can be expressed as [48],

$$\nabla \cdot \mathbf{E} = 0, \qquad \nabla \cdot \mathbf{H} = 0, \tag{4.1}$$

$$\nabla \times \mathbf{E} = i\mu\Omega\mathbf{H}, \qquad \nabla \times \mathbf{H} = -i\Omega\epsilon\mathbf{E}. \tag{4.2}$$

Where Ω is the frequency of that field. From which we can derive the vector wave equation.

$$\nabla^2\mathbf{E} + k^2\mathbf{E} = 0, \qquad \nabla^2\mathbf{H} + k^2\mathbf{H} = 0, \tag{4.3}$$

where $k = \omega^2\epsilon\mu$ is the wave vector. We can try the following set of solutions to Maxwell's equation

$$\mathbf{M} = \nabla \times (\mathbf{c}\psi), \qquad \mathbf{N} = \nabla \times \frac{\mathbf{M}}{k}, \tag{4.4}$$

where $\mathbf{c}$ is a constant vector and ψ is a scalar function. The divergence of a curl is zero by definition, which means that Eq. (4.1) is satisfied by construction. We can use the vector identity

$$\nabla \times \nabla^2\mathbf{A} = -\nabla \times \nabla \times \nabla \times \mathbf{A} = \nabla^2\nabla \times \mathbf{A}, \tag{4.5}$$

to show that

$$\begin{aligned} \nabla^2\mathbf{M} + k^2\mathbf{M} &= \nabla \times \mathbf{c}(\nabla^2\psi + k^2\psi), \\ \nabla^2\mathbf{N} + k^2\mathbf{N} &= \nabla \times \nabla \times \mathbf{c}/k(\nabla^2\psi + k^2\psi). \end{aligned} \tag{4.6}$$

This means that both $\mathbf{M}$ and $\mathbf{N}$ satisfy the vector wave equation,

$$\nabla^2\mathbf{M} + k^2\mathbf{M} = 0, \qquad \nabla^2\mathbf{N} + k^2\mathbf{N} = 0, \tag{4.7}$$

if ψ satisfies the scalar wave equation,

$$\nabla^2\psi + k^2\psi = 0. \tag{4.8}$$

Combining (4.5) and(4.7) $\nabla \times \mathbf{N} = k\mathbf{M}$ so that $\mathbf{N}$ and $\mathbf{M}$ fulfil all requirements for the electromagnetic field. This reduces the problem to finding solutions to solving the scalar wave equation. To match the symmetry of the problem we can take $\mathbf{M} = \nabla \times (\mathbf{r}\psi)$ where $\psi(\theta, \phi, r)$ are solutions to the scalar wave equation. By using seperation of variable its possible to find solutions of the form $\psi = R(r)\Theta(\theta)\Phi(\phi)$. It can be shown (Bohren and Huffman, pp.85 [48]) that a complete set of solutions to the scalar wave equation can be generated with

$$\psi_{emn} = \cos(m\phi)P_n^m(\cos\theta)z_n(kr), \tag{4.9}$$

$$\psi_{omn} = \sin(m\phi)P_n^m(\cos\theta)z_n(kr), \tag{4.10}$$

where P_n^m are Legendre polynomials and $z_n(kr)$ can be spherical Bessel functions of the first 3 kinds(Appendix A.1). The o/e subscript denotes an odd or even function and m and n are separation constants. The spherical vector harmonics generated by these functions are given by

$$\mathbf{M}_{omn/emn} = \nabla \times (\mathbf{r}\psi_{omn/emn}), \tag{4.11}$$

$$\mathbf{N}_{omn/emn} = \nabla \times (\frac{\mathbf{M}_{omn/emn}}{k}). \tag{4.12}$$

Which are complete set of solutions to the vector wave equation. In our experiment we have an incident plane wave that is scattered on a spherical particle,

$$\mathbf{E_i} = E_0 e^{ikr\cos(\theta)}\hat{\mathbf{e}}_x. \tag{4.13}$$

Incoming plane waves can be expanded in vector spherical harmonics, which results in

$$\mathbf{E_i} = \sum_{m=0}^{\infty}\sum_{n=m}^{\infty}(B_{emn}\mathbf{M}_{emn} + B_{omn}\mathbf{M}_{omn} + A_{emn}\mathbf{N}_{emn} + A_{omn}\mathbf{N}_{omn}). \tag{4.14}$$

It is possible to calculate the expansion coefficients using that all solutions generated by Eq. 4.11 and Eq. 4.12 are mutually orthogonal [48],

$$\frac{\int_0^{2\pi}\int_0^{\pi}\mathbf{E_i}\cdot\mathbf{M}_{emn}\sin(\theta)\mathrm{d}\theta\mathrm{d}\phi}{\int_0^{2\pi}\int_0^{\pi}|\mathbf{M}|^2_{emn}\sin(\theta)\mathrm{d}\theta\mathrm{d}\phi} = \frac{\int_0^{2\pi}\int_0^{\pi}B_{emn}\mathbf{M}_{emn}\cdot\mathbf{M}_{emn}\sin(\theta)\mathrm{d}\theta\mathrm{d}\phi}{\int_0^{2\pi}\int_0^{\pi}|\mathbf{M}|^2_{emn}\sin(\theta)\mathrm{d}\theta\mathrm{d}\phi} = B_{emn}. \tag{4.15}$$

By filling in an incoming plane wave for the incident beam

$$\frac{\int_0^{2\pi}\int_0^{\pi}E_0 e^{ikr\cos(\theta)}\hat{\mathbf{e}}_x\cdot\mathbf{M}_{emn}\sin(\theta)\mathrm{d}\theta\mathrm{d}\phi}{\int_0^{2\pi}\int_0^{\pi}|\mathbf{M}|^2_{emn}\sin(\theta)\mathrm{d}\theta\mathrm{d}\phi} = B_{emn}. \tag{4.16}$$

As a plane wave is finite in the origin and Bessel functions of the second kind are infinite in the origin, Bessel functions of the first kind are used for z_n in Eq. 4.9. After some calculations of the coefficients(all terms with $m \neq 1$ are zero) we end up with

$$\mathbf{E_i} = E_0 \sum_{n=1}^{\infty} \frac{i^n(2n+1)}{n(n+1)}(ia_n\mathbf{M}_{o1n}^{(1)} - b_n\mathbf{N}_{e1n}^{(1)}), \tag{4.17}$$

$$\mathbf{H_i} = \frac{-k}{\Omega\mu}E_0 \sum_{n=1}^{\infty} \frac{i^n(2n+1)}{n(n+1)}(ib_n\mathbf{M}_{e1n}^{(1)} - a_n\mathbf{N}_{o1n}^{(1)}), \tag{4.18}$$

where the superscripts denote the kind of spherical Bessel associated with $z_n$in Eq. 4.9. The next step is to also expand the scattered and internal fields in vector spherical harmonics. We have the following boundary conditions at the surface of the particle

$$(\mathbf{E_i} + \mathbf{E_s} - \mathbf{E_l}) \times \hat{\mathbf{e}}_r = (\mathbf{H_i} + \mathbf{H_s} - \mathbf{H_l}) \times \hat{\mathbf{e}}_r = 0. \tag{4.19}$$

Based on the orthogonality of the vector harmonics and the boundary conditions it is possible to show that the expansion of the scattered field in spherical vector harmonics is given by

$$\mathbf{E_s} = \sum_{n=1}^{\infty} E_0 \frac{i^n(2n+1)}{n(n+1)}(ia_n\mathbf{N}_{eln}^{(3)} - b_n\mathbf{M}_{oln}^{(3)}), \tag{4.20}$$

$$\mathbf{H_s} = \frac{-k}{\Omega\mu}E_0 \sum_{n=1}^{\infty} \frac{i^n(2n+1)}{n(n+1)}(ib_n\mathbf{M}_{e1n}^{(1)} + a_n\mathbf{N}_{o1n}^{(1)}). \tag{4.21}$$

The expansion of the field inside the particle is given by

$$\mathbf{E_l} = E_0 \sum_{n=1}^{\infty} \frac{i^n(2n+1)}{n(n+1)}(c_n\mathbf{M}_{o1n}^{(1)} - id_n\mathbf{N}_{e1n}^{(1)}), \tag{4.22}$$

$$\mathbf{H_i} = \frac{-k}{\Omega\mu} \sum_{n=1}^{\infty} E_0 \frac{i^n(2n+1)}{n(n+1)}(d_n\mathbf{M}_{e1n}^{(1)} + ic_n\mathbf{N}_{o1n}^{(1)}). \tag{4.23}$$

After expanding all the fields in spherical vector harmonics we can use boundary conditions to calculate scattering coefficients a_n and b_n

$$\mathbf{E_i} + \mathbf{E_s} = \mathbf{E_l}, \qquad \mathbf{H_i} + \mathbf{H_s} = \mathbf{H_l}. \tag{4.24}$$

which results in

$$a_n = \frac{\mu_1 m^2 j_n(mx)\frac{\delta(xj_n(x))}{\delta x} - \mu_1 j_n(x)\frac{\delta(mxj_n(mx))}{\delta x}}{\mu m^2 j_n(mx)\frac{\delta(xh_n^{(1)}(x))}{\delta x} - \mu h_n^{(1)}(mx)\frac{\delta(mxj_n(mx))}{\delta x}}, \tag{4.25}$$

$$b_n = \frac{\mu_1 j_n(mx)\frac{\delta(xj_n(x))}{\delta x} - \mu_1 j_n(x)\frac{\delta(mxj_n(mx))}{\delta x}}{\mu j_n(mx)\frac{\delta(xh_n^{(1)})(x)}{\delta x} - \mu h_n^{(1)}(x)\frac{\delta(mxj_n(mx))}{\delta x}}. \tag{4.26}$$

Where $h_n^{(i)}$ are spherical Bessel functions of the third kind also known as Hankel functions of the first or second kind (see Eq. A.5), $x = \frac{2\pi r_{\text{particle}}}{\lambda} n_{\text{medium}}$ is the size parameter, $r_{particle}$ is the radius of the particle and $m = \frac{n_{\text{particle}}}{n_{\text{medium}}}$ is the relative refractive index.

According to Bohren and Huffmann pp.111 [48] the series in Eq. 4.20 is convergent and the size parameter $x = 2\pi a/\lambda$ is a rough estimate of the amount of terms needed in the expansion to get an accurate approximation of the scattered field. The code used in this thesis cuts off the expansion after $n_c = 2 + x + x^{1/3}$ terms. If $kr >> n_c$, which is true at the location of the detector, the Hankel functions can be approximated by

$$h_n^{(1)} = -i^n e^{ikr}, \qquad h_n^{(2)} = i^n e^{-ikr}, \tag{4.27}$$

$$E_{s\theta} = E_0 \frac{e^{ikr}}{-ikr} \cos\phi S_2(cos\theta), \tag{4.28}$$

$$E_{s\phi} = -E_0 \frac{e^{ikr}}{-ikr} \cos\phi S_1(cos\theta). \tag{4.29}$$

Where S_1 and S_2 are elements of the scattering amplitude matrix and are given by,

$$\begin{aligned} S_1 &= \sum_{n=1}^{n_c} \frac{2n+1}{n(n+1)} (a_n \frac{P_n^1}{sin(\theta)} + b_n \frac{\mathrm{d}P_n^1}{\mathrm{d}\theta}), \\ S_2 &= \sum_{n=1}^{n_c} \frac{2n+1}{n(n+1)} (a_n \frac{\mathrm{d}P_n^1}{\mathrm{d}\theta} + b_n \frac{P_n^1}{sin(\theta)}), \end{aligned} \tag{4.30}$$

$$\begin{pmatrix} E_{\parallel s} \\ E_{\perp s} \end{pmatrix} = \frac{e^{ikr}}{-ikr} \begin{pmatrix} S_2 & 0 \\ 0 & S_1 \end{pmatrix} \begin{pmatrix} E_{\parallel i} \\ E_{\perp i} \end{pmatrix}. \tag{4.31}$$

Here the subscripts of E indicate the components of the scattered and incident field that are parallel and perpendicular with respect to the scattering plane. We can now calculate the scattered field as a function of the size of particle and wavelength, we now only need a suitable quantity that we can measure that depends strongly on the size parameter.

Consider the light scattered at a 90° angle to the incoming beam. If the particle is very small, it is close to the dipole regime. The dipole moment will align with the polarisation of the probe beam. Because a dipole does not radiate in the direction of its dipole moment, the intensity of the light scattered towards the camera when the polarisation of the incident beam is parallel to the scattering plane will be zero while it will be maximal when the polarisation of the incident beam is perpendicular to the scattering plane. Now for very large particles the dipole moment will be very small, and as the particle is likely roughly spherically symmetric the scattering will be independent of the polarisation of the probe beam. Looking at Equation (4.31) $|S_2|^2$ and $|S_1|^2$ are proportional to the intensity of the light scattered with a parallel

or perpendicular polarised probe beam respectively. This suggests that the visibility could be a reasonable parameter to characterise the size of the particle, the visibility in interference patterns is usually defined as

$$V_{\text{fringe}} = \frac{I_{max} - I_{min}}{I_{max} + I_{min}} \tag{4.32}$$

which is positive by definition, however a slightly different definition will be used here,

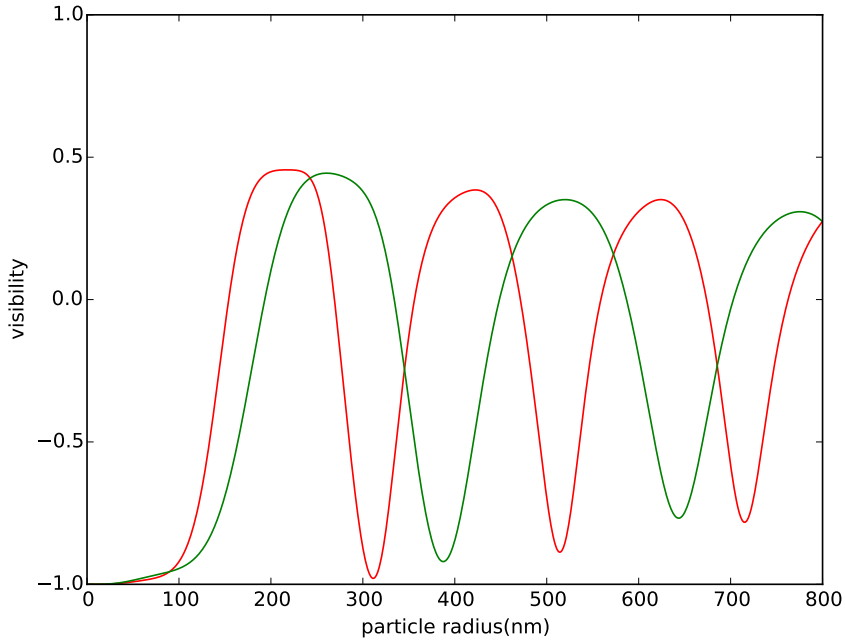

Figure 4.1: Theory curves based on Mie theory, numerical calculted visibility(defined in Eq. 4.33) as a function of particle radius, for 2 different wavelengths.

$$V = \frac{|S_2|^2 - |S_1|^2}{|S_1|^2 + |S_2|^2}. \tag{4.33}$$

This expression is similar to how the visibility is normally defined, however as it is signed it carries information about whether a parallely polarised incident beam corresponds with a maximum or a minimum of the intensity scattered at a 90°angle with respect to the incident beam. In this research we use the pymiecoated code [49] which is based on the procedure described in Bohren and Huffmann (Appendix A and B [48]). The particle size for two different wavelengths have been calculated and plotted in Fig. 4.1. Because a single value for the visibility corresponds to various size values, it will be impossible to unambiguously assign a single radius for a given

wavelength and visibility. However by probing with a number of different wavelengths, it should be possible to uniquely determine the particle size by comparison of the locations of the intersections.

5 Polarimetry Setup

To measure the visibility required for determining the size of the particles a polarimetry setup is needed. The setup can be seen in Fig. 5.1.

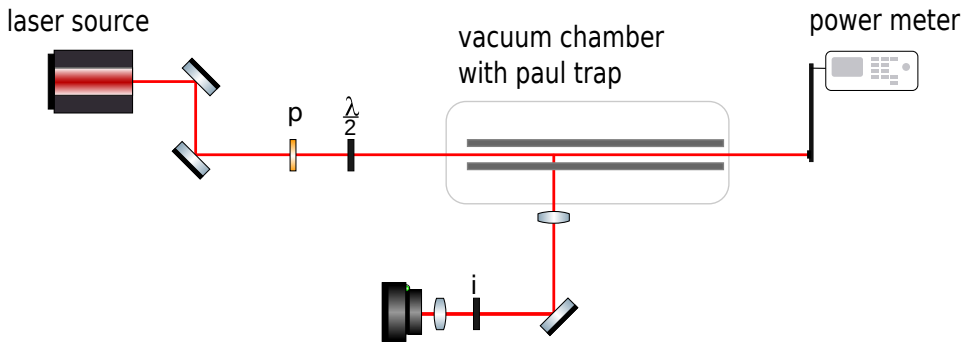

Figure 5.1: Setup for the polarimetry measurements. A probe laser goes through a linear polariser p and a half waveplate. The probe beam scatters on particles in the trap and the scattered light is collected by the imaging system(f1= 180 mm and f2= 50 mm). An iris is used between f1 and f2 to reduce the numerical aperture. Transmitted light is collected by a power meter that is used to compensate if the power output is not constant throughout the experiment

As discussed in Sec. 4, polarimetry with a single probe laser will give an ambiguous result. Therefore lasers with different wavelengths are needed to determine the size. We used a number of different laser source setups, two of which will be discussed in this thesis. In a first experiment we used a Helium-Neon laser (633 nm) and a diode laser (785 nm). In a second experiment a setup three diode lasers(642 nm, 785 nm and 852 nm) was used, in this setup, the lasers are connected to single mode fibers. A three wavelength division multiplexer combines these three fibers into a fiber that is single mode for all three wavelengths. A linear polariser ensures the incident beam is linearly polarised. In the second measurement a polarisation controller that squeezes the fiber is used to maximise the linearity of the polarisation of the light that is leaving the multiplexer. This is done to increase the transmission through the polariser. The polarisation of the outgoing beam is changed as the stress caused by this squeezer changes the birefringence of the fiber. Then we use a superachromatic half-wave plate (SAHWP05M-700) to rotate the direction of the polarisation of the incident probe beam. This beam is aligned through the holes in the endcaps onto a power meter which we use to calibrate fluctuations in laser power. After scattering on the particles they are imaged with a 4-f system(f1 = 180 mm, f2 = 50 mm) onto a Point Grey Grasshopper 3 camera (GS3-U3-51S5M-C) with a resolution of 2440x2048 and a pixel size of 3.4 µm. Because the numerical Mie theory calculations that we have done are only exactly correct for a 90° scattering angle, an iris is placed in between the two lenses to reduce the numerical aperture. The particles scatter

over the full solid angle and for light that scatters at non-90°angles with respect to the incident beam, the polarisation dependency that we base our measurement on decreases. As such we want to reduce the numerical aperture of our detection system, so a larger fraction of the light we collect at the camera was scattered near a 90°angle.

6 Results

6.1 Results for the Helium Neon Laser and the 785nm Diode Laser in a Vacuum

Using the setup described in Sec. 5 . A measurement cycle of a 100 pictures was done at each of those polarisation angles. The shutter time during these measurements was 100 ms. A typical picture taken by the camera is shown in Fig. 6.1, where five particles and two of rods can be seen and particles are enumerated for future reference. To reduce the signal to noise ratio regions of interests were chosen around a single particle. See for example Fig. 6.2, here we define $\phi_{\text{polarisation}}$ as the angle of the polarisation of incident beam with the scattering plane. The z-axis of this region of interest is chosen to be an order of magnitude larger then the y-axis. This was done because large scale oscillations were common on that axis. In x and y axes the particles are tightly trapped and any motions in those directions were too small to resolve.

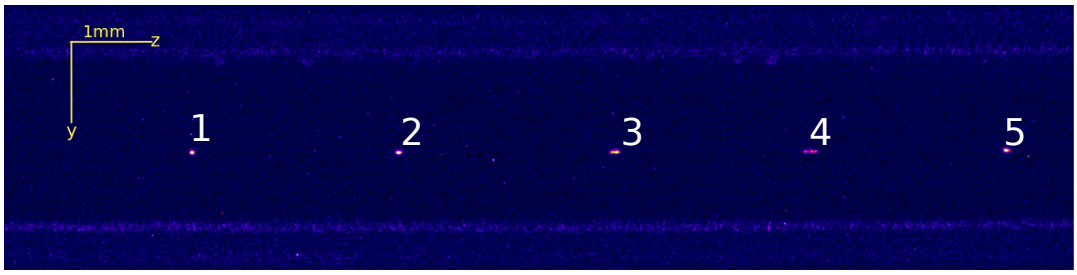

Figure 6.1: A false-colour image of the light scattered on five gold nanospheres. The particles were probed with a Helium-Neon laser with a polarisation that is at an 8 ° angle with respect to the scattering plane. On the top and the bottom of the image the electrode rods of the trap are visible. The particles are enumerated for future reference.

We sum the image in the y-direction to obtain a 1D array and use Gaussian functions to fit this array, as shown in Fig. 6.3. Using the parameters from the fit, the Gaussian function are analytically integrated to obtain the total signal from each particle in the image.

In about 10% of the images there are multiple maxima, as can be seen in Fig. 6.2b.

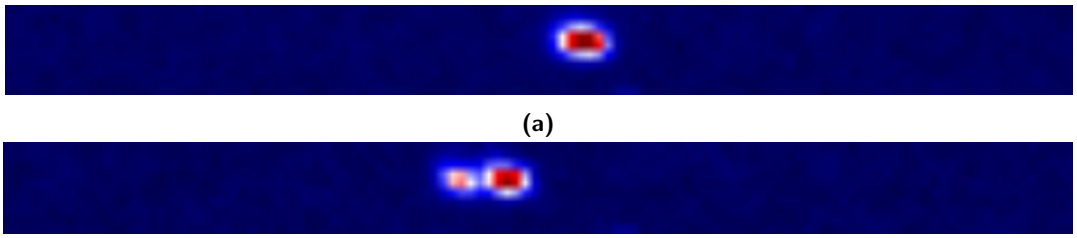

(a)

(b)

Figure 6.2: Examples of regions of interest pictures, using a Helium-Neon laser. The incident beam had a polarisation angle $\phi_{\text{polarisation}}$ of 8 °with respect to the scattering plane. **a**) shows a zoomed in image of particle 5 in Fig. 6.1). **b**) shows an image of the same particle depicted at a later time. The particle has two maxima, likely due to the fact that the particles are oscillating.

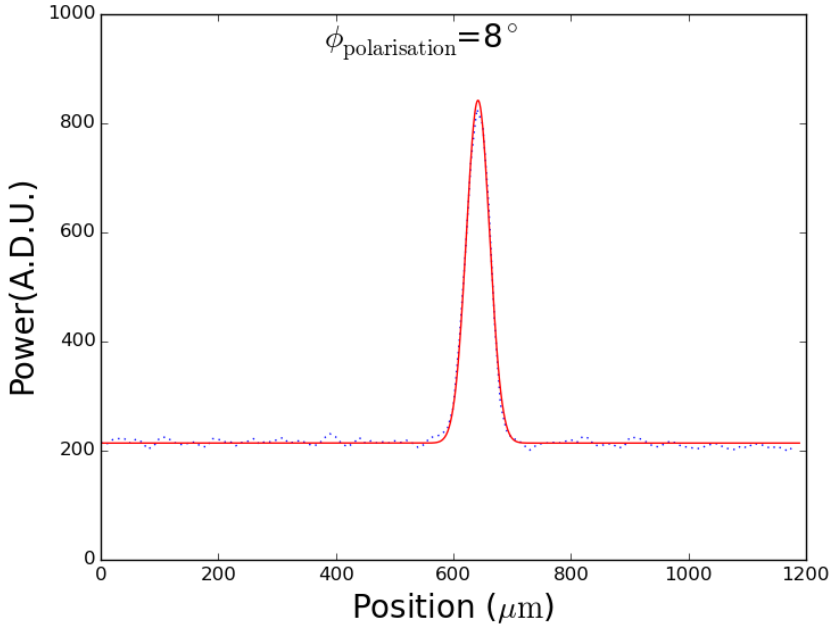

Figure 6.3: Power scattered(in analog digital units) by particle 1 at a single time for $\phi_{\text{polarisation}} = 8°$, This graph were made by summing all pixel values from the region of interest Fig. 6.2 in the y direction. a Gaussian function is fitted through the resulting graph

Presumably this is due to oscillations of the particles as the velocity should be the lowest near the turning points. It is unlikely to be a dumbbell shaped aggregate as they are to small to resolve with our optical system . We used the sum of two Gaussian functions to fit these double peaks, as shown in Fig. 6.4 . The scattering amplitude should be independent of time. The standard deviations for these two methods are shown in Tab. 6.1. Considering that all the standard deviations are lower while using a summed Gaussian function, that method seems to improve the

fits. From these graphs we can retrieve the visibility as described in section 5.

A weighted average for each angle was taken over the scattered power that was obtained by integrating the Gaussian functions,

$$\mu_x = \frac{\sum_i (x_i w_i)}{\sum_i w_i}, \qquad \sigma_\mu^2 = \frac{1}{\sum_i w_i}, \tag{6.1}$$

where the sum is over all measurements at a single angle, where μ_x is the mean power scattered by a particle at a single angle, x_i is the value of measurement i, σ_i is the fit uncertainty of a measurement i, $w_i = 1/\sigma_i^2$ is the weight of a measurement i, and σ_μ is the standard deviation of the mean. In Fig. 6.5 and the figures in appendix B the average scattered power as a function of incident polarisation angle as can be seen. A sinusoidal function is used to fit the data. The error bars are based on the standard deviation σ_μ of the mean.

The measured visibilities are listed in Tab. 6.2. These visibilities and their uncertainties are compared to Mie theory in Figs. 6.6-6.8 (this Mie theory curve was calculated in Fig. 4.1). We can make a maximum likelihood estimate for the particle size. Every possible particle size has a theory prediction of the visibility for all wavelengths. We can use a probability density as a function of visibility based on the gaussian distributions defined by the measured visibilities and their standard deviations to assign a probability density for each size. By multiplying these probability densities for each wavelength we get a maximum likelihood estimate for the particle size. The distributions are shown in Fig. 6.10, and the most likely values are shown in 6.3. Note that the values for these distributions are very low, especially for particles 2 and 4, which indicates that this data does not seem to fit the theory well .

	particle 1	particle 2	particle 3	particle 4	particle 5
Diode, Gaussian function	9.4%	9.8%	6.2%	8.6%	7.5%
Diode, two Gaussian functions	8.2%	9.2%	5.5%	8.2%	6.8%
Helium-Neon, Gaussian function	8.0%	7.4%	6.0%	6.6%	7.1%
Helium-Neon, two Gaussian functions	7.1%	6.5%	5.2%	5.4%	6.1%

Table 6.1: Average standard deviation of a 100 picture measurement cycle as a percentage of the average scattered power for both lasers. The standard deviation while only using a single Gaussian function to fit the data is compared with using the sum of two Gaussian functions to fit the data

	particle 1	particle 2	particle 3	particle 4	particle 5
785 nm diode laser visibility	0.099	0.031	0.117	-0.107	0.114
785 nm diode laser standard error	0.009	0.006	0.006	0.004	0.004
Helium-Neon laser visibility	0.058	0.021	0.218	-0.119	0.259
Helium-Neon laser standard error	0.006	0.007	0.006	0.007	0.006

Table 6.2: Visibilities and corresponding standard error of the particles. These are calculated using the amplitude and offset extracted from sinusoidal fits like the ones shown in Fig. 6.5. The visibility is defined in Equation 4.33. Note that this is different from the definition that is more commonly used as it has a sign.

	particle 1	particle 2	particle 3	particle 4	particle 5
Most likely radius	466 nm	465 nm	577 nm	342 nm	577 nm
σ	2 nm	1 nm	2 nm	1 nm	2 nm

Table 6.3: Most likely radius for each particle Fig. 6.10, uncertainties only include the statistical error.

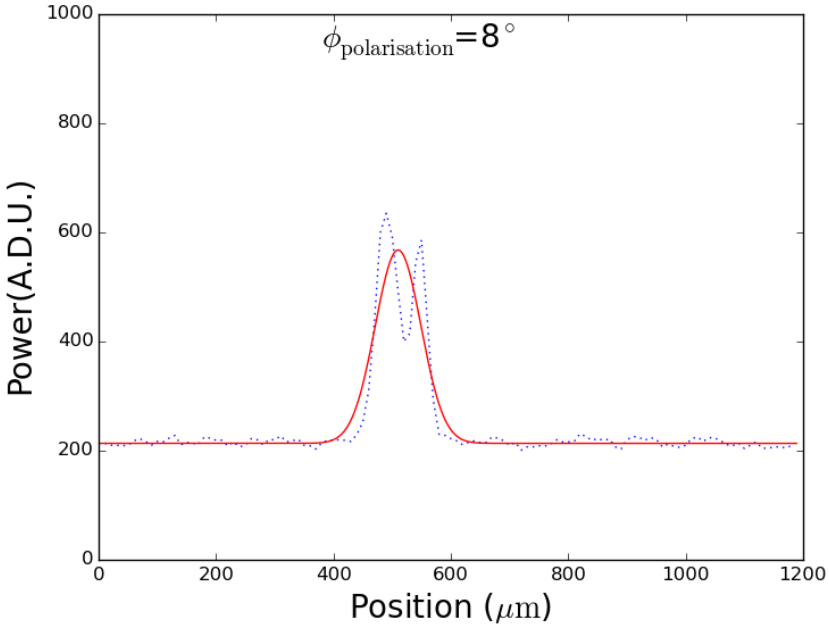

(a)

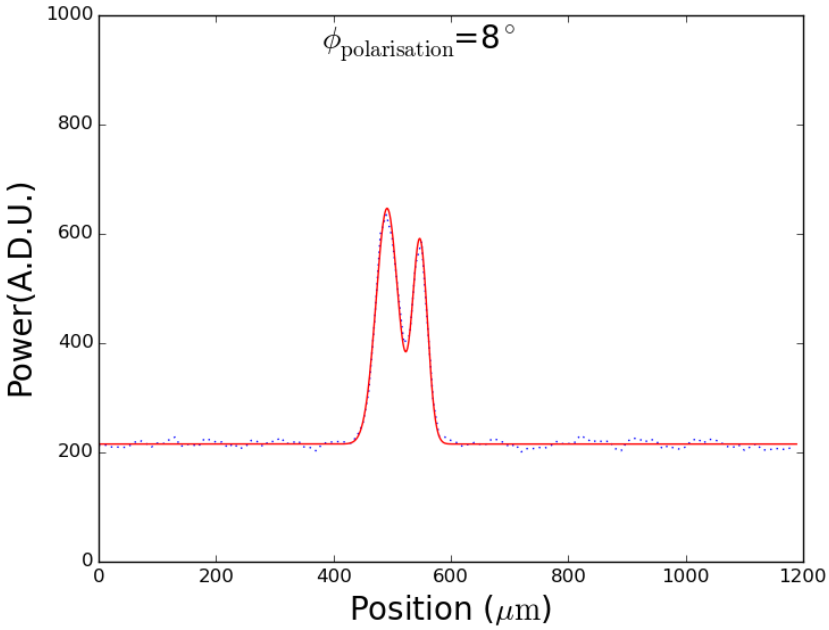

(b)

Figure 6.4: Power scattered by particle 5, a single Gaussian function has been fitted through **a**) and the sum of two Gaussian functions have been fitted through **b**), both images are from the same picture as Fig. 6.2b

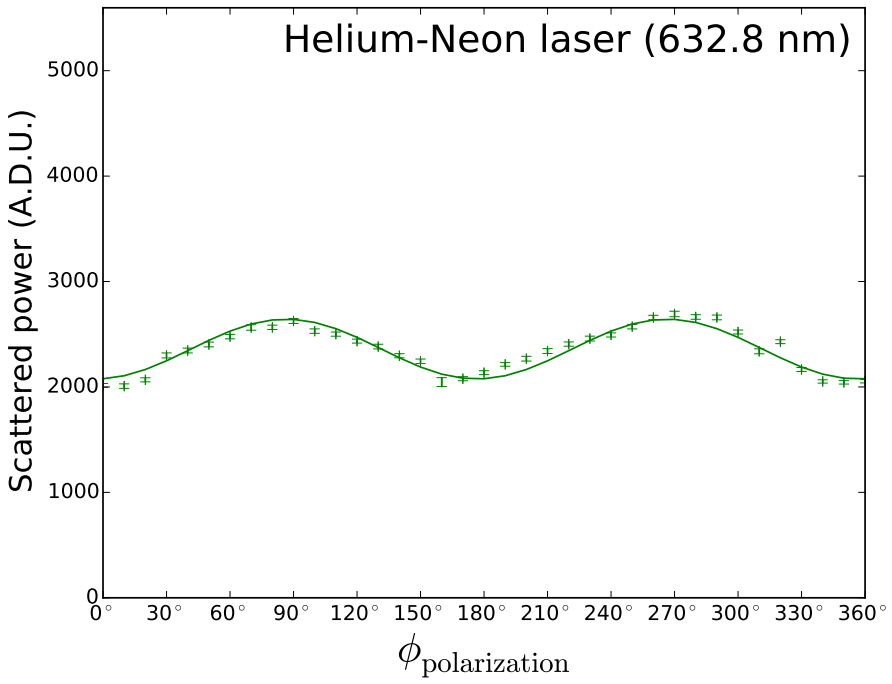

(a)

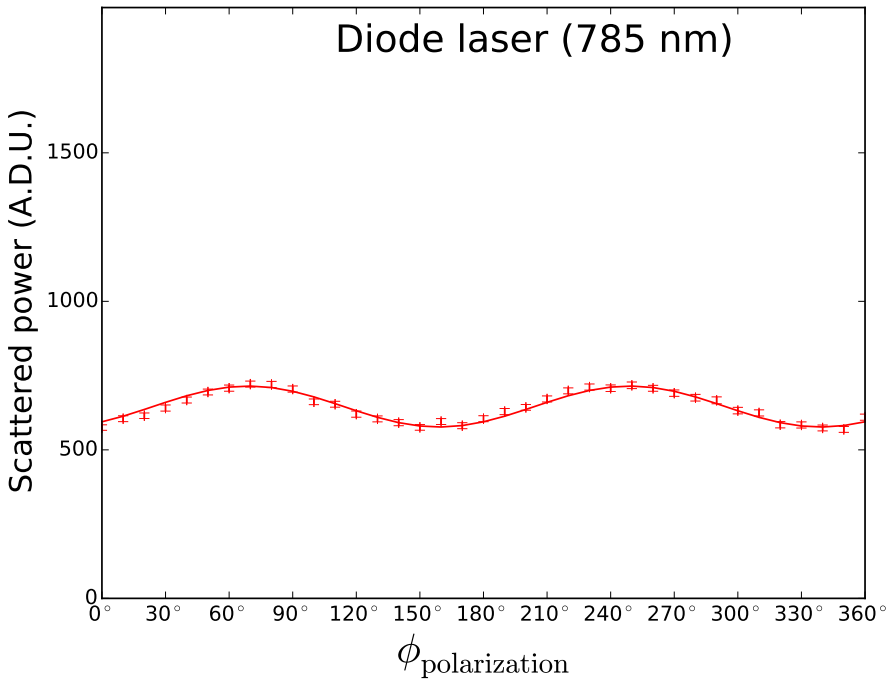

(b)

Figure 6.5: Average power scattered by the particle 5 as a function of the angle of the polarisation of the incident beam. **a**) shows a measurement with the Helium-Neon laser($632.8\,\text{nm}$) and **b**) shows a measurement with a diode laser ($785\,\text{nm}$). The other particles are shown in the appendix B.1.

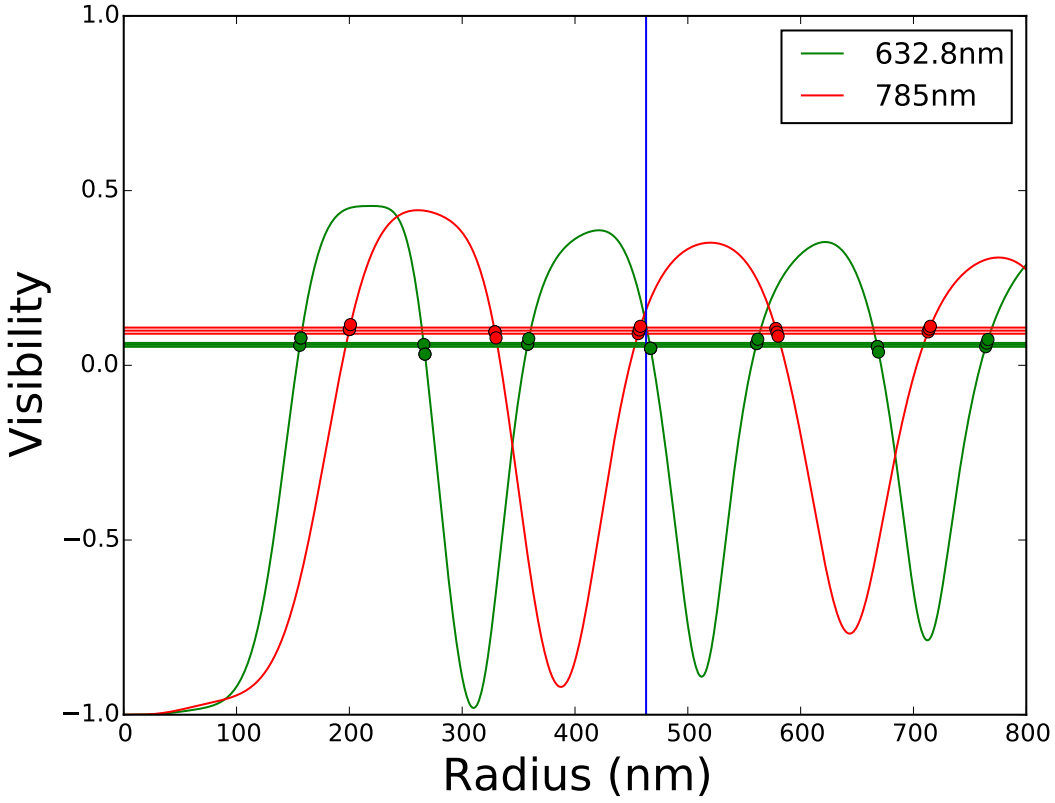

Figure 6.6: Comparison of the measured visibilities with Mie theory. The horizontal lines represent the measured visibilities (Tab. 6.2) and their standard error. The theoretical curves are based on Mie theory and the circles denote intersection between the data and the theory for a single wavelength, this graph shows particle 1. The vertical lines indicate the most likely radius.

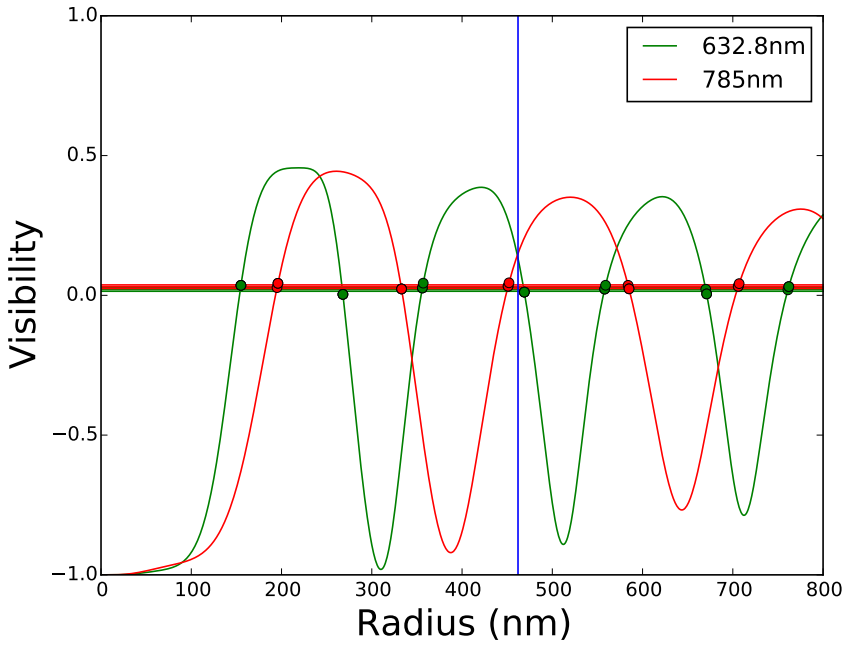

(a)

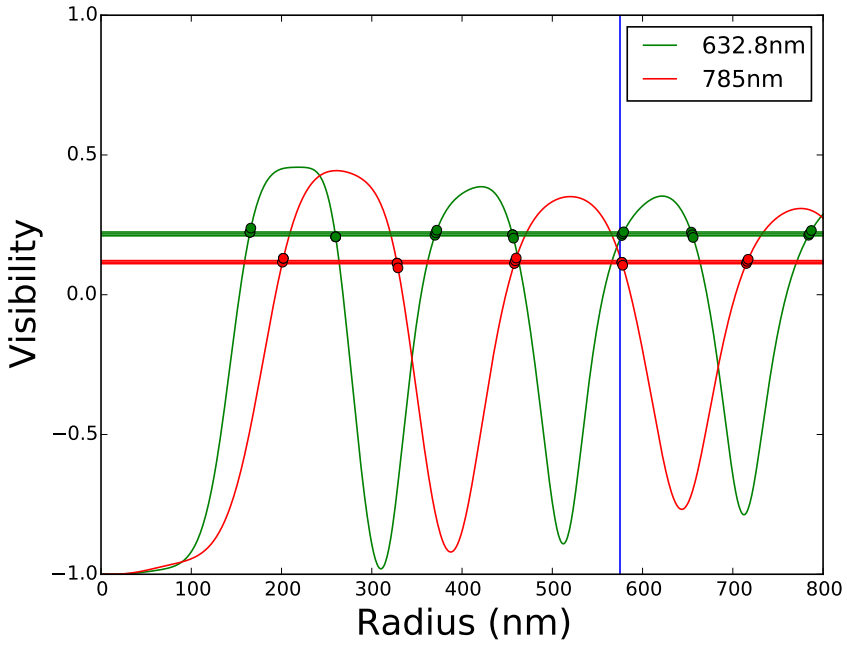

(b)

Figure 6.7: Comparison of the measured visibilities with Mie theory. The horizontal lines represent the measured visibilities (Tab. 6.2) and their standard error. The theoretical curves are based on Mie theory and the circles denote intersection between the data and the theory for a single wavelength. **a**)shows particle 2 and **b**)shows particle 3. The vertical lines indicate the most likely radius.

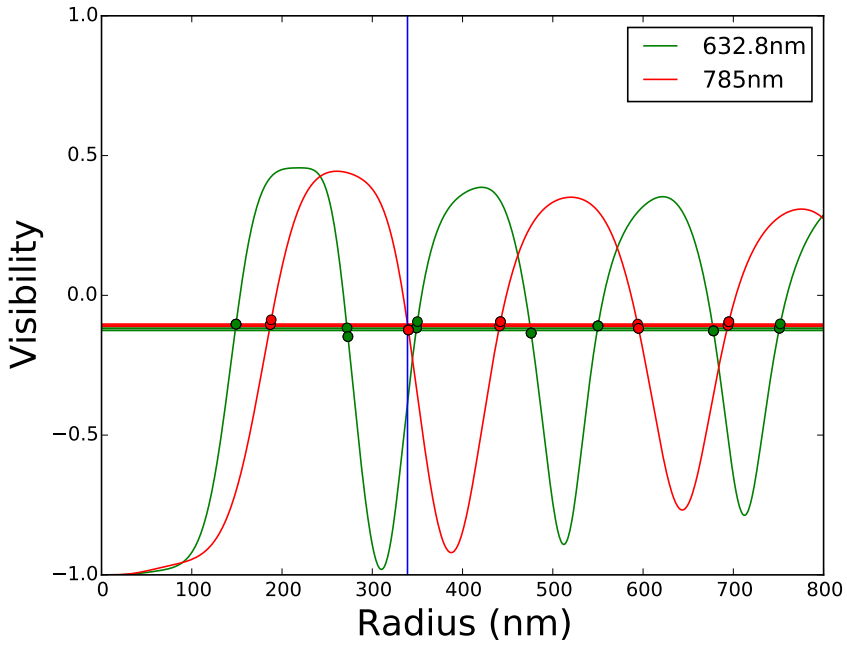

(a)

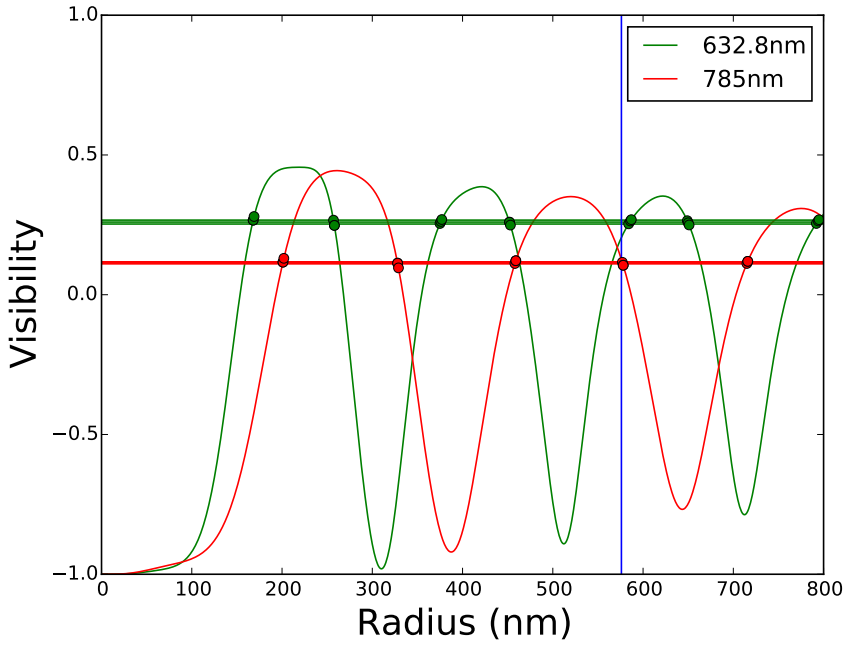

(b)

Figure 6.8: Comparison of the measured visibilities with Mie theory. The horizontal lines represent the measured visibilities(Tab. 6.2) and their standard error. The theoretical curves are based on Mie theory and the circles denote intersection between the data and the theory for a single wavelength. **a**)shows particle 4 and **b**)shows particle 5. The vertical lines indicate the most likely radius.

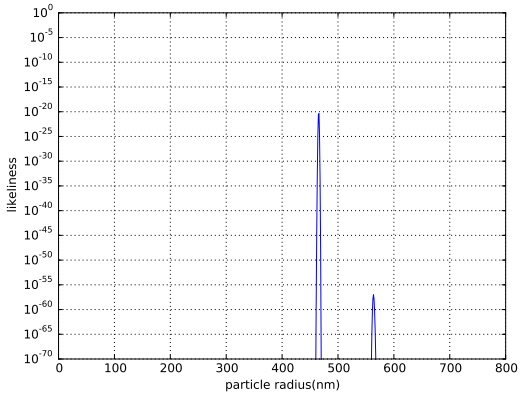

(a) particle 1

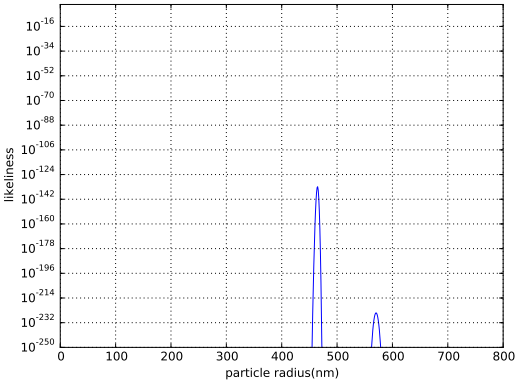

(b) particle 2

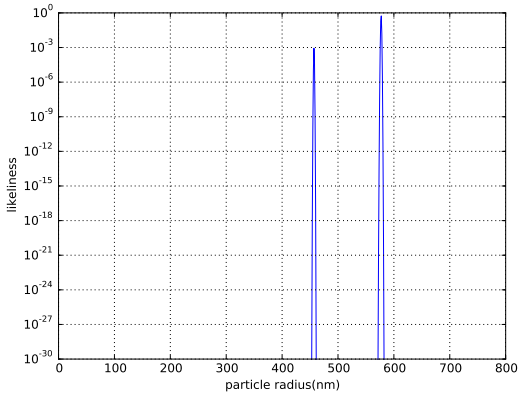

(a) particle 3

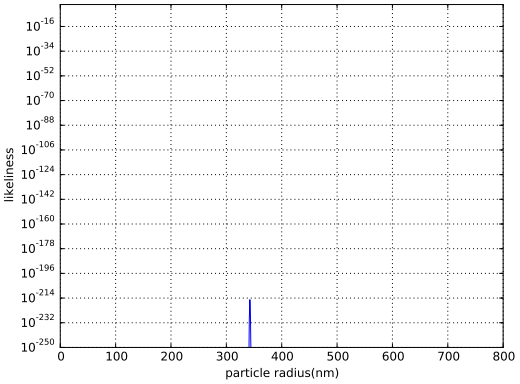

(b) particle 4

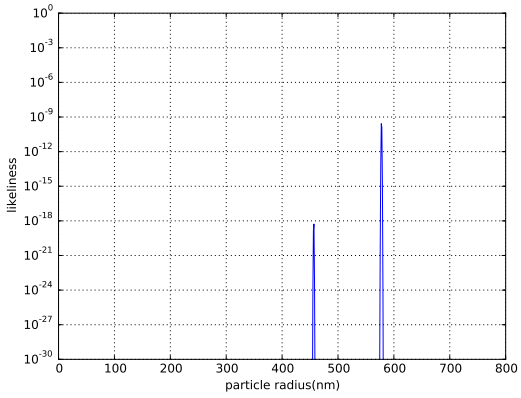

(c) particle 5

Figure 6.10: Likelihood distribution as a function of particle size. This gives a measure of the best estimate of the radius. The differences in scales on the y-axis are many order of magnitude.

6.2 Results for Measurements with Three Diode Lasers at Atmospheric Pressure

In the second experiment measurements were preformed with three diode lasers with wavelengths of 642 nm, 785 nm and 852 nm. Unlike the measurements described in the previous section, this experiment was done at atmospheric pressure due to technical reasons. This had a few consequences on the measurement. Fast oscillations on the z-axis were damped to a point that the double maxima as described in Fig. 6.2b were no longer observable. However, thermal motion on the y-axis was observed. Compared to the setup in the previous system the alignment was improved, the mirrors were adjusted to make sure that the imaged particles scatter their lights closer to a 90°angle then those in an earlier experiment. The shutter time was set to 250 ms which allowed for further reducing the numerical aperture using the iris while maintaining the signal to noise ratio. As discussed in Sec. 5 reducing the aperture increases the visibility, as a larger fraction of the scattered light collected on the camera is scattered near a 90°angle.

The first measurements were done with the 785 nm laser. An image taken of the light scattered by the particles is shown in Fig. 6.12, particles from this experiment are not the same as the first experiment, however they are from the same batch of trapped particles, the process in obtaining the data is described in more detail in Sec. 6.1.

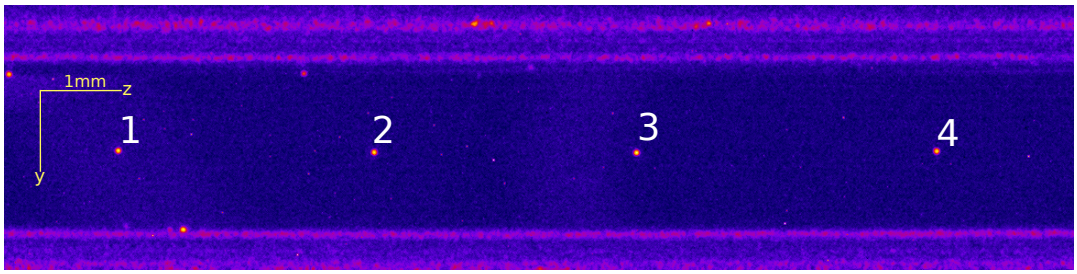

Figure 6.11: An image of the light scattered on four gold nanospheres. Here the particles were probed with a 785 nm laser with a polarisation that is perpendicular to the scattering plane. On the top and the bottom of the image the electrode rods of the trap are visible. The particles are enumerated for future reference.

The average scattered power as a function of incident polarisation angle is retrieved as described in the previous Sec. 6.1 and can be seen in Fig. 6.12, the corresponding visibilities can be seen in Tab. 6.4.

Comparing these visibility values to the results of the first measurement 6.2, the visibilities measured in the second measurement are on average a factor three higher then those of the first measurement with the same laser. It is worth mentioning here that another measurement with these three diode lasers has been done before im-

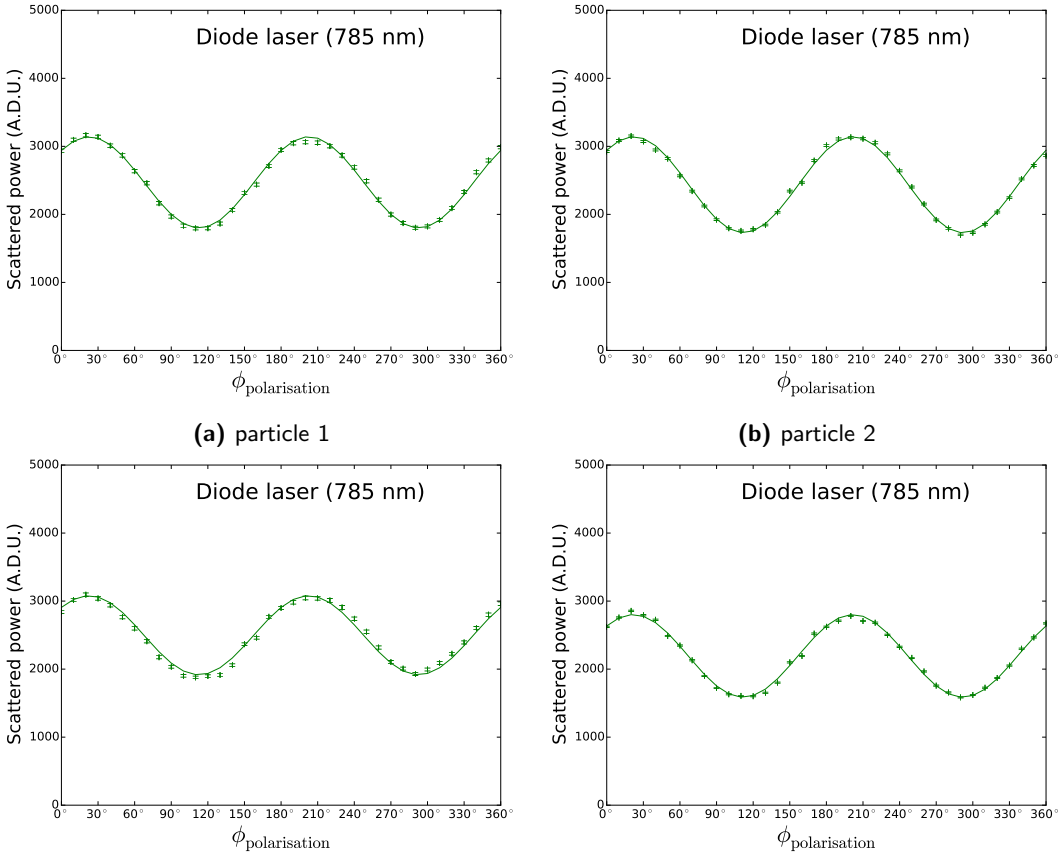

(a) particle 1 **(b)** particle 2

(c) particle 3 **(d)** particle 4

Figure 6.12: Scattered power as a function of the polarisation angle of the incident beam, each point in the graph is the weighted average (Eq 6.1) of a 100 images the wavelength of the laser used in these measurements was 785 nm and a sinusoidal function is fitted through these points.

plementing the improvements discussed earlier in this section. This measurement yielded very low visibilities for all wavelengths and a point of overlap could not be found for all three until very large particle sizes. Therefor we suspect we have been underestimating the visibility in all earlier measurements. As the slope of the theory curves is much steeper at low visibilities then at high visibilities, its unlikely for measurements with many different wavelengths to all show low visibilities for the same particles.

After that, measurements were done with with the 642 nm diode laser. Unfortunately when the particles were probed with this laser and 1.6 mW transmission through the chamber, particles started moving on the long axis of the trap. Therefore the particles measured with the 642 nm and 852 nm diode lasers are likely not the same particles as those measured with the 785 nm diode laser. However as the results of these measurements indicate that the particles in this region seem to be-

	particle 1	particle 2	particle 3	particle 4
785 nm Diode laser visibility	0.271	0.289	0.232	0.276
785 nm Diode laser visibility standard error	0.004	0.004	0.006	0.004

Table 6.4: visibilities extracted from Fig6.12 and corresponding standard error.

have very similar to each other, we will assume for now that the particles are similar enough that the results obtained for the four particles of the first measurement can be used in conjunction with the results for the other two lasers. As can be seen in Fig. 6.13, the particles have travelled large distances during both these experiments. In the measurement with the with the 852 nm diode laser, the particles appear to be drifting back to their old equilibrium positions .

In Fig. 6.14 the power scattered by the particles as a function of polarisation angle for 640 nm and 852 nm lasers is plotted. The scattered power measured on the camera appears to decrease linearly for 642 nm. To compensate for this downward slope, $f(t) = (1 - b\phi)(\text{amplitude } \sin(2\ \phi - \Delta\phi) + c)$ has been used as function to fit the data instead of a normal sinusoidal function. The visibility is retrieved by $V = \pm\text{amplitude}/c$, where the sign is positive if the maximum is at polarisation parallel to the scattering plane, and negative if the maximum is perpendicular to the scattering plane.

In Fig. 6.15 the data of the three measurements is compared to the theory. As it is unlikely that one of the particles of the measurement with the 785 nm diode laser correspond to one of the two particles of the two other measurements, the visibilities found for that experiment are averaged and the estimated uncertainty is increased by the standard deviation of that average, to account for the spread in particle sizes.

	particle 1	particle 2
642 nm Diode laser visibility	0.27	0.29
642 nm Diode laser standard error	0.01	0.01
784 nm Diode laser visibility	0.37	0.44
784 nm Diode laser standard error	0.01	0.01

Table 6.5: visibilities extracted from Fig. 6.14 using Eq 4.33 and corresponding standard error.

As we have done for the first experiment we can do a maximum likelihood estimation to get a best guess for the size of the particles. In Fig. 6.16 the probability distribution as a function of particle radius is shown, giving us a most likely particle size for both particles in Tab. 6.6.

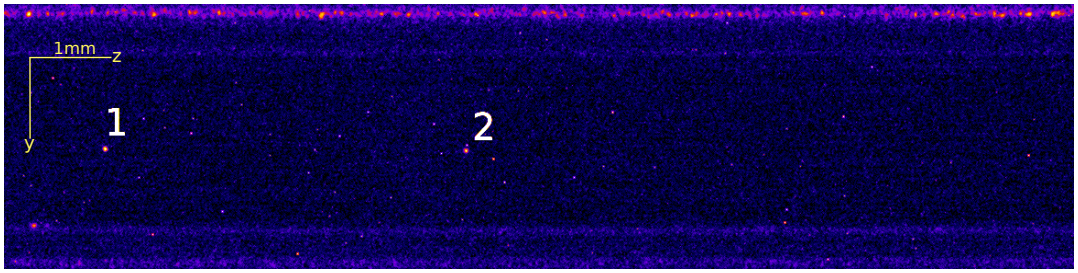

(a)

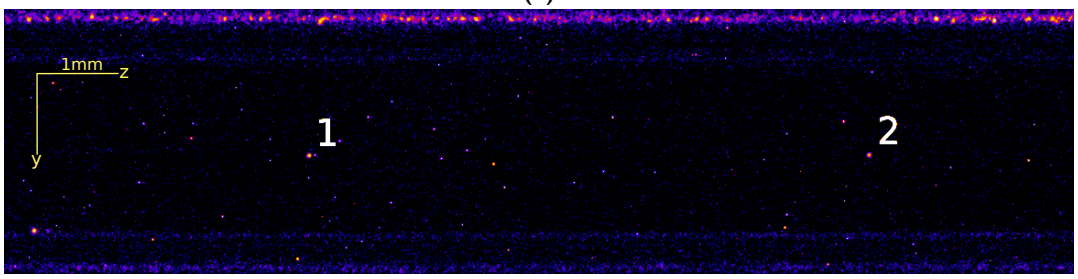

(b)

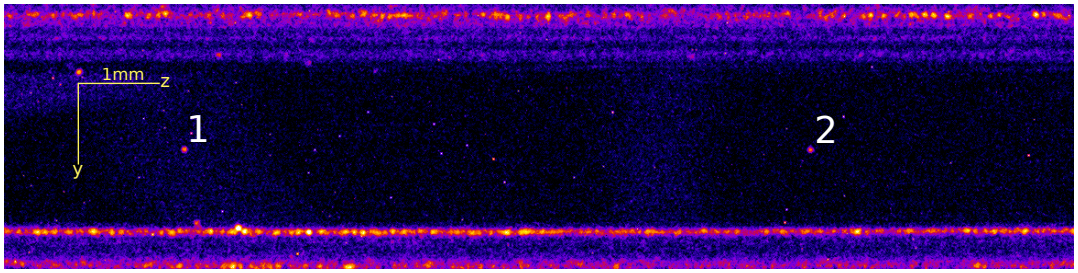

(c)

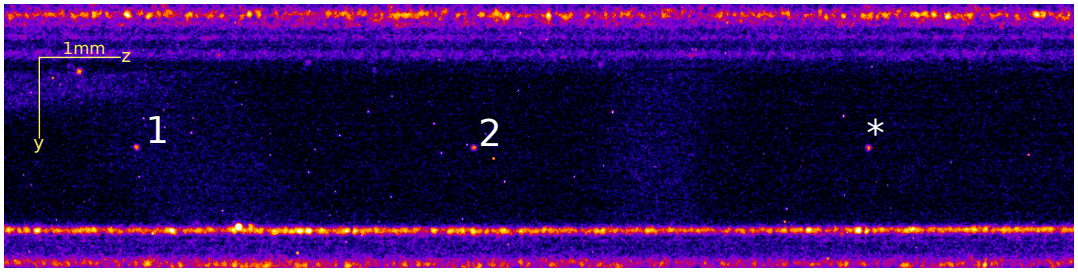

(d)

Figure 6.13: An image of the scattered light of two gold nanospheres. On the top and the bottom of the image the electrode rods of the trap are visible. An image is shown from both the start and the end of both measurements. The particles are enumerated for future reference, the particle denoted with a star is not tracked as it is not present in all frames, **a**) shows an image made at the start of the 642 nm measurement, **b**) shows an image made at the end of the 642 nm measurement, **c**) shows an image made at the start of the 852 nm measurement, **d**) shows an image made at the end of the 852 nm measurement.

	particle 1	particle 2
Most likely particle size	177 nm	174 nm
σ	1 nm	1 nm

Table 6.6: Maximum likely radius for both particles, based on Fig.6.16.

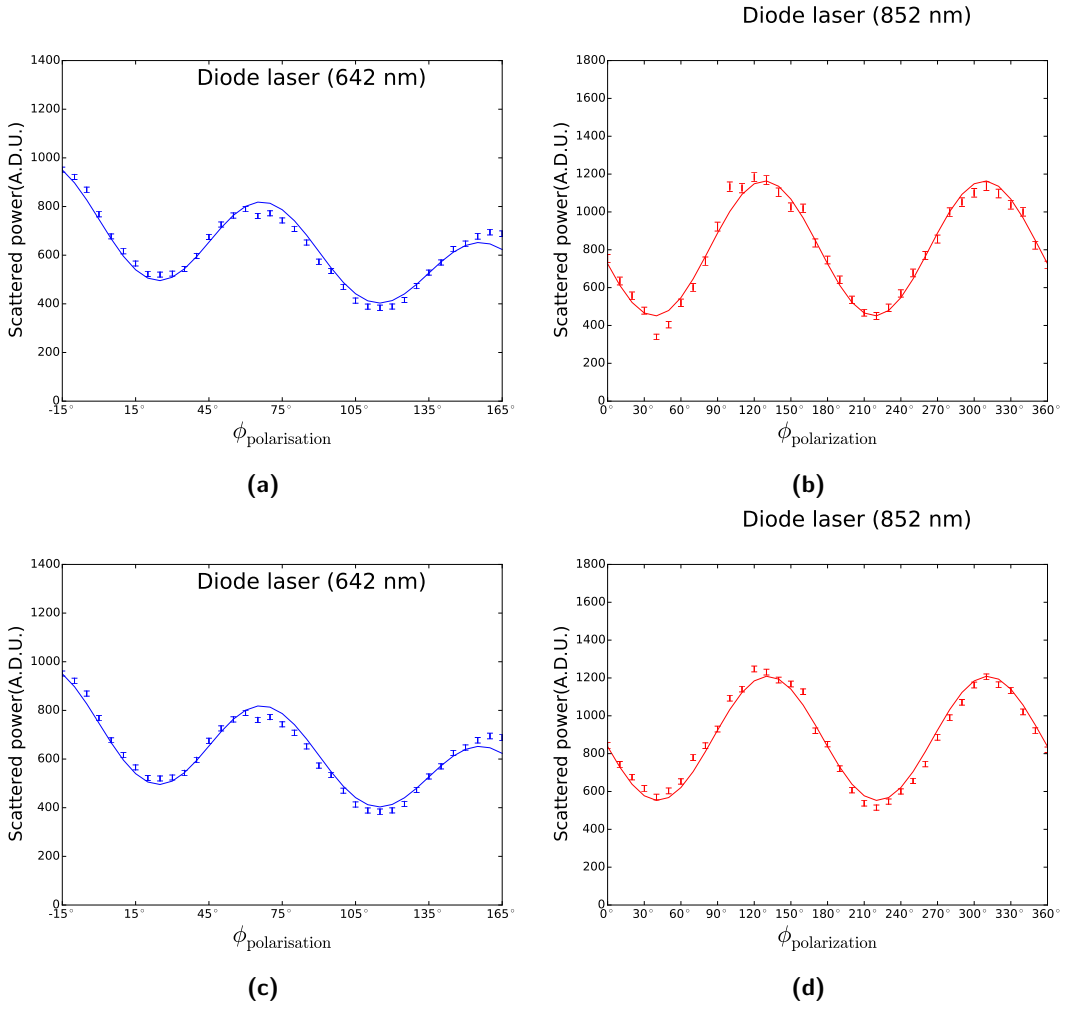

Figure 6.14: Scattered power as a function of the polarisation angle of the incident beam. **a**) shows particle 1 from Fig. 6.13 with the 642 nm diode laser, **b**) shows particle 1 with the 852 nm diode laser, **c**) shows particle 2 with the 642 nm diode laser,**d**) shows particle 2 with a 642 nm diode laser.

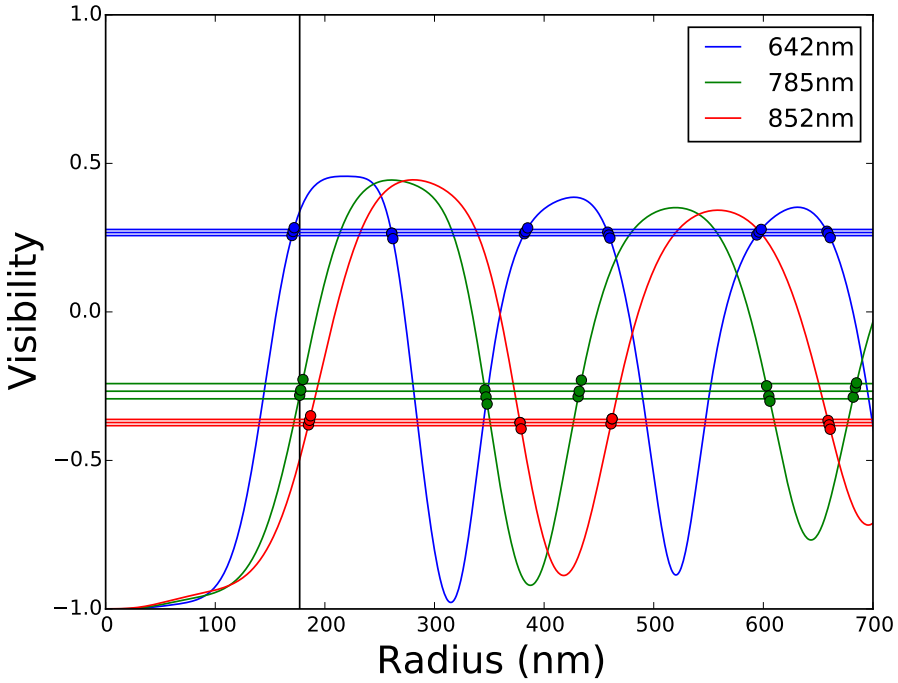

(a) particle 1

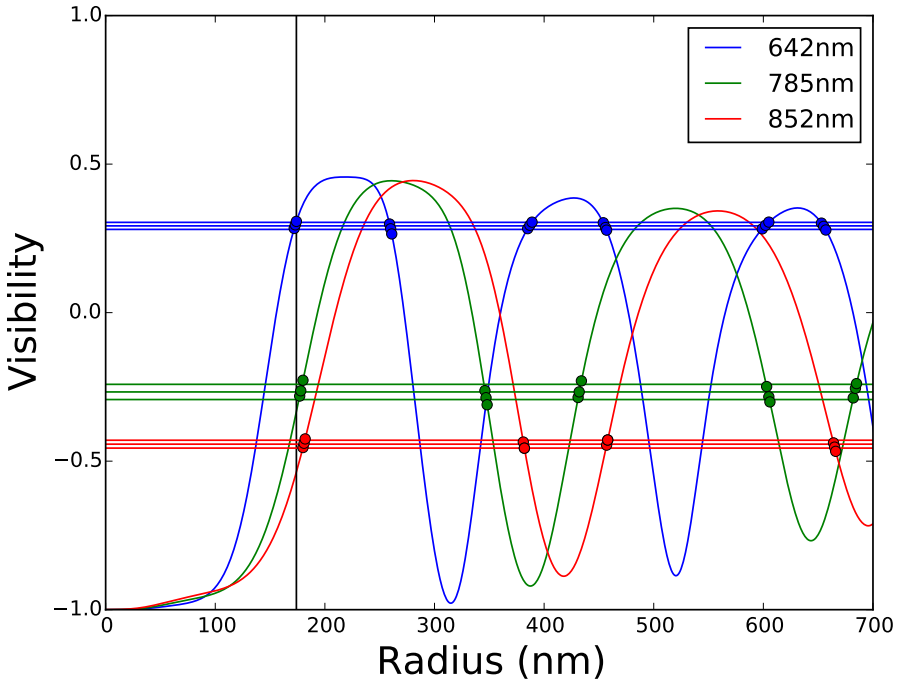

(b) particle 2

Figure 6.15: comparison of the Mie theory with the data for the three diode laser measurement. The horizontal lines denote the measured visibility and its uncertainty, while the dots indicate intersections between the theory and the data. The vertical line indicates the most likely radius.

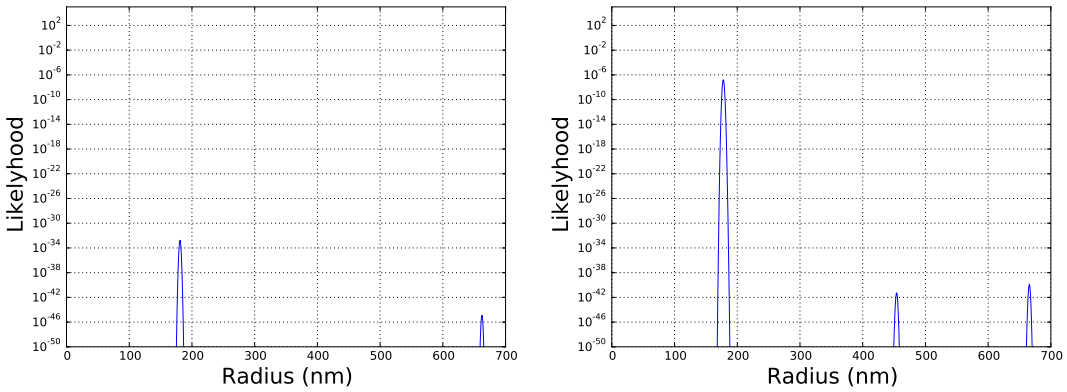

(a) particle 1 **(b)** particle 2

Figure 6.16: Likelihood distribution as a function of particle size, this gives a measure of the best estimate of the radius.

7 Conclusion and Discussion

We have used electrospray ionisation to charge and separate gold nanospheres. We have successfully trapped these nanoparticles in a Linear Ion Trap for extended periods of time. We have investigated polarimetry measurements as a method to do in-situ measurements of the size of these particles. For this purpose we have done two experiments. For the first setup we have used a Helium-Neon laser and a 785 nm laser diode to probe the particles in the trap. For the second experiment we used three diode lasers (642 nm , 785 nm and 852 nm). The size of the particles is extracted by measuring the polarisation dependence of light scattering at a 90°angle with the incident beam. This dependence was compared to numerical calculations based on Mie theory for scattering on homogeneous spheres.

The results of the measurement of the Helium Neon laser seem to indicate radii between 342 nm and 577 nm as shown in Tab. 7.1. Fig. 6.6, Fig. 6.7a and Fig. 6.8a as well as Fig. 6.10 show that these data are in poor agreement with the theory for at least three out of five particles, as the intersections between the theory and the data overlap poorly for all possible radii. For particle 3 and especially particle 5 the intersections between the theory and the data have better overlap at a radius of 577 nm, note that the uncertainties given here only consist of the statistical error. However there is a reasonable chance this is just coincidence. There are many crossings between the theory curves and the visibilities that were measured. Therefore there is a reasonable chance that the intersections with the theoretical curves will overlap somewhere, even if the theory does not properly describe the data.

	particle 1	particle 2	particle 3	particle 4	particle 5
Maximum likelihood	466 nm	465 nm	577 nm	342 nm	577 nm
σ	2 nm	1 nm	2 nm	1 nm	2 nm

Table 7.1: Most likely radius for each particle, for the experiment with the Helium-Neon laser and a 785 nm diode laser

To get more conclusive results we switched to a setup that uses three different diode probe lasers.The third laser reduces the chance that the shared intersection is a coincidence. With this setup we found that based on our data and the theory the most likely particle size for the particles is shown in Tab. 7.2. The overlap in Fig. 6.15 is fairly reasonable for particle 2 and fairly bad for particle 1. As the particles were moving rapidly during this experiment and as we had to adjust for a linear decrease of the scattered intensity over time, it is likely that some systematic error is obtained.

The values found for the radius in the second experiment are significantly different from the most likely particle sizes we found in the first experiment. While both experiments used a 785 nm laser measurement, the visibilities found for that wavelength during the second experiment are much larger then those in the first experi-

	particle 1	particle 2
Most likely particle size	177 nm	174 nm
σ	1 nm	1 nm

Table 7.2: Maximum likely radius for both particles, based on Fig.6.16

ment. This means that either the particles we have imaged in the two experiments have a radically different sizes or the visibility found in at least one of the measurements is incorrect.

By eye and in figures 6.1 and 6.11 the inter-particle spacing seems almost constant throughout the trap. This makes large variations in charge very unlikely. Considering the trap is charge to mass ratio selective, this also makes large size variations quite unlikely. Which suggests that at least one of these measurements is likely either overestimating or underestimating the visibility. It seems unlikely that an effect would cause overestimate the polarisation dependence of the scattering compared to another experiment on similar particles. On the other hand, there are arguments that might explain the low visibilities found in the first experiment. In the dipole picture it is clear that the visibility is reduced if the particles do not scatter at a 90°angle with respect to the incoming beam. The particles imaged in the first experiment where more to the sides of the trap and where not scattering at a 90°angle, which reduces their visibility. Optimisation with the squeezer and a higher output power of the laser allowed us to close the iris from 8 mm to 2 mm. This reduced the numerical aperture of the imaging system which increased the visibility of particles in focus. Therefore we suspect that we have underestimated the visibility in the first measurement. In conclusion we deem the values from the second experiment considerably more likely then those of the first measurement, especially because the measurements of the first experiment were made with only two lasers. More measurements will have to be done to conclusively say if this is a feasible method. However as the results of the second experiment are reasonably close to the theory considering the large-scale movements on the z-axis and the downward slope of the intensity in the measurement with the 642 nm diode laser, this could be a feasible method to do in-situ measurements on the radius of the particles.

8 Outlook

The eventual goal of the research is ablation of single gold particles. To achieve this goal, more experiments must be done to verify whether the size analysis method is accurate.

A new vacuum chamber will be implemented. The current chamber had relatively limited optical access. The new chamber will be fully transparent in the yz-plane and the xz-plane. This might allow the investigation of the scattered intensity as a function of scattering angle.

The uniform ground rods in our current linear ion trap will be replaced by segmented rods. By attaching these segments to D.C. power source it is possible to tune the potential on the rods, which allows us to seperatly move particles around in the trap. This solves a number of different problems.

- When we ablate these particles we can use the segments to move particles into the path of the ablation beam.
- We can prevent large scale movements on the long axis, which will restrain the particles from moving out of the trap.
- The lattice spacing between charged particles is determined by the equilibrium of the constraining segmented rod field and the repulsive force particles exert on each other,. This allows us to calculate the charges of the particles by measuring the lattice spacing. As the trapping conditions are dependent on the charge to mass ratio, it is possible to measure the particle size in an independent way.

All particles currently trapped seem to be aggregates. Therefore improvements to the electrospray and trapping methods have to be made to minimise the number of aggregates that will be trapped.

- Particles tend to stick to the walls, as PVP is sometimes used as an adhesive for gold to fused silica [47]. This could be a source of aggregation. New particles are blocked which will create aggregates that grow until the surface of the aggregate is large enough the pressure of the flow overtake the adhesive forces. This can likely be solved by coating the glass with a layer of PVP or by using gold particles that are coated with a different stabiliser.
- The electrospray method is charge to mass selective. the path of small particles with a high charge to mass ratio will be deflected more. By spraying at an angle, only particles with a sufficiently high charge to mass ratio's will be deflected enough to reach the entrance of the trap.

- Another way to selectively remove larger particles would be by using the right trap parameters. The dimensionless friction coefficient κ in Eq. 2.9 scales inversely with the mass and that scales with r^3. The potential terms in this equation scale with the charge to mass ratio. If we assume the amount of charge scales with the surface of the colloid, the charge to mass ratio scales inversely with r. By finding the regime were the Cunningham correction factor is relatively small but the friction is still important, one can achieve a situation where the stability region of small particles is relatively large due to damping while the stability region of large particles is relatively small. This is illustrated in the stability zones of Fig. 8.1.

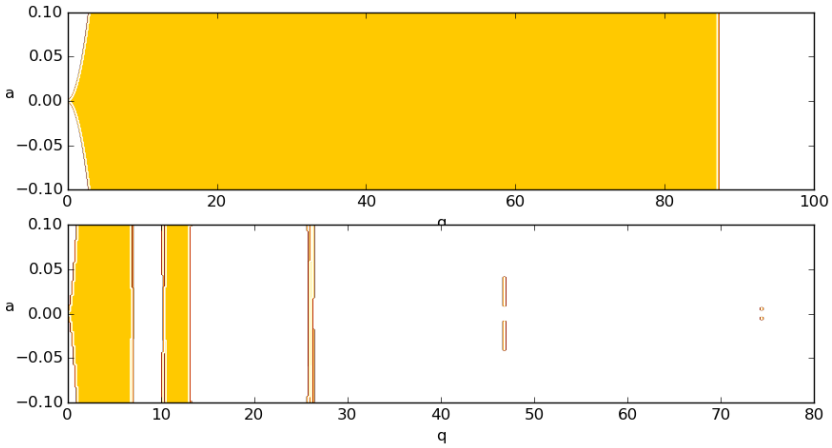

Figure 8.1: A comparison of the stability of two particles with a different radii as a function of the trap parameters. The pressure in these calculations is 3000 Pa and the trap frequency is 300 Hz. The yellow area's indicate stability, the top graph shows a stability zone for a particle with a radius of 50 nm and the bottom graph shows a stability zone for a particle with a radius of 150 nm .

Appendix A Functions

Spherical Bessel functions of the first kind are defined as,

$$j_n(z) = \sqrt{\pi/(2z)} J_{n+1/2}(z), \tag{A.1}$$

where,

$$J_n(z) = \frac{\Sigma_{\ell=0}^{\infty}(-1)^{\ell}}{2^{2\ell+m}\ell!(m+1)!} z^{2\ell+n}, \tag{A.2}$$

are Bessel functions of the first kind. Spherical Bessel functions of the second kind are defined as,.

$$y_n(z) = \sqrt{\pi/2z} Y_{n+1/2}(z), \tag{A.3}$$

where,

$$Y_n(z) = \frac{J_n(z)\cos(n\pi) - J_{-n}(z)}{\sin(n\pi)}, \tag{A.4}$$

are Bessel functions of the second kind. Spherical Bessel functions of the third kind also called Hankel functions of the first and second kind are given by,

$$h_n^{(1)} = j_n + iy_n, \tag{A.5}$$

$$h_n^{(2)} = j_n - iy_n. \tag{A.6}$$

The associated Legendre Polynomials are given by,

$$P_{\ell}^{m}(x) = (-1)^m (1-x^2)^{m/2} \frac{\mathrm{d^m} P_{\ell}(x)}{\mathrm{d}x^m}. \tag{A.7}$$

where

$$P_{\ell}(.x) = \frac{1}{2^{\ell}\ell!} \frac{\mathrm{d}^{\ell}(x^2-1)^{\ell}}{\mathrm{d}x^m} \tag{A.8}$$

are ℓ order Legendre polynomials.

Appendix B Data

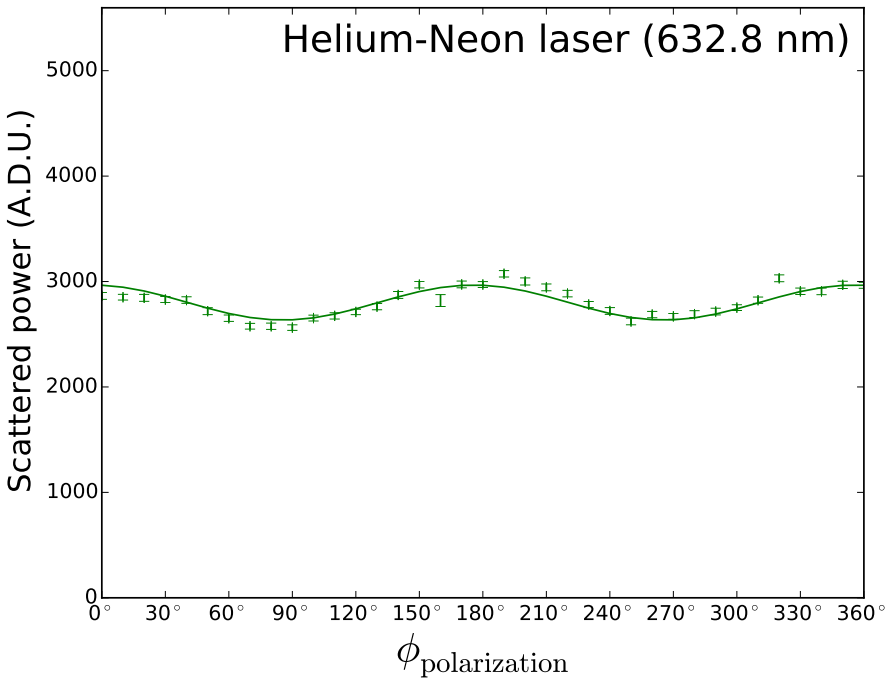

(a)

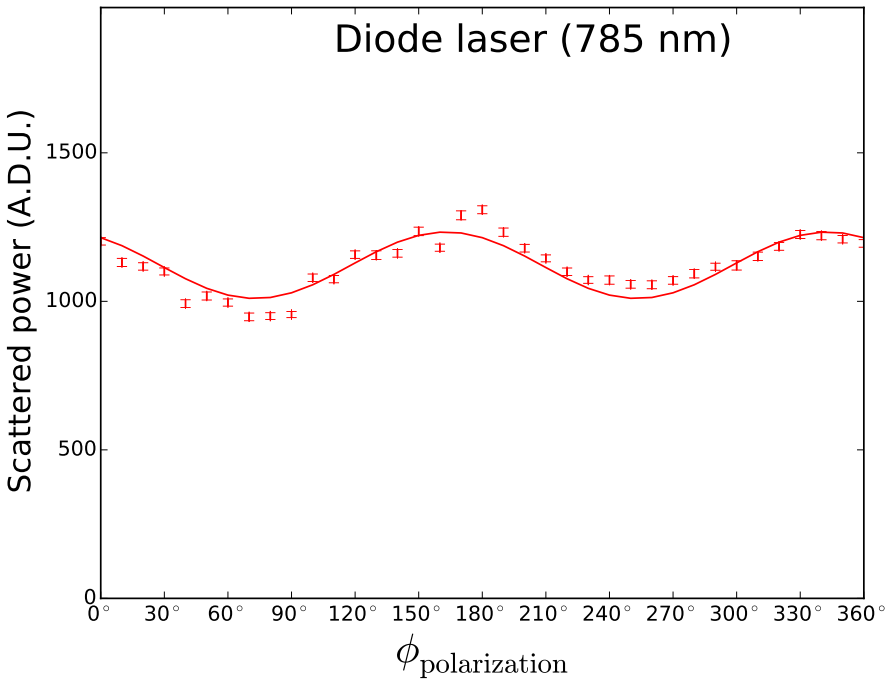

(b)

Figure B.1: Average scattered power as a function of the polarisation angle for particle 1 in the first measurement, see Fig. 6.5. **a**) shows a measurement with a Helium-Neon laser and **b**) shows a measurement with a 785 nm diode laser.

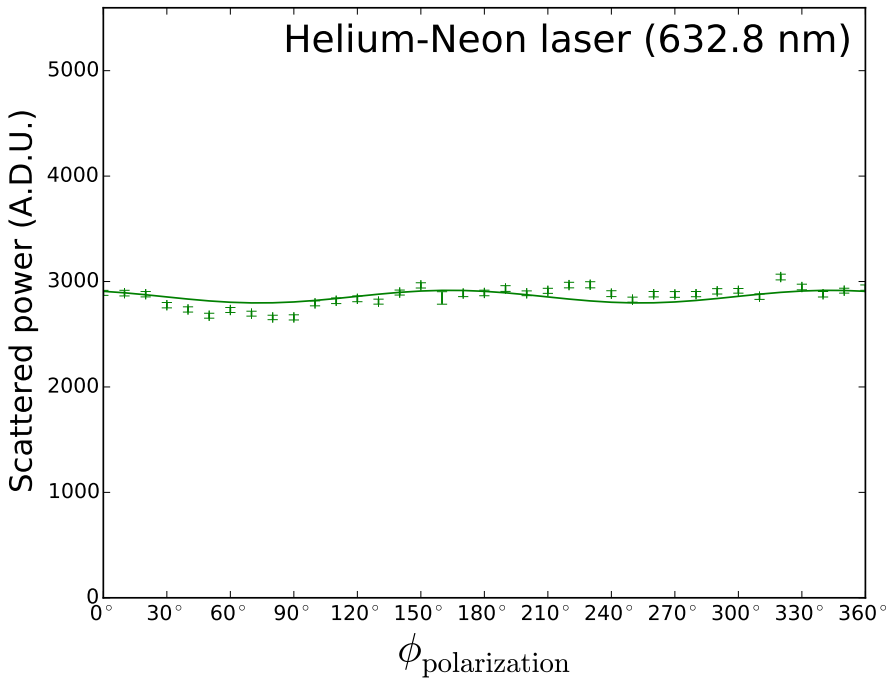

(a)

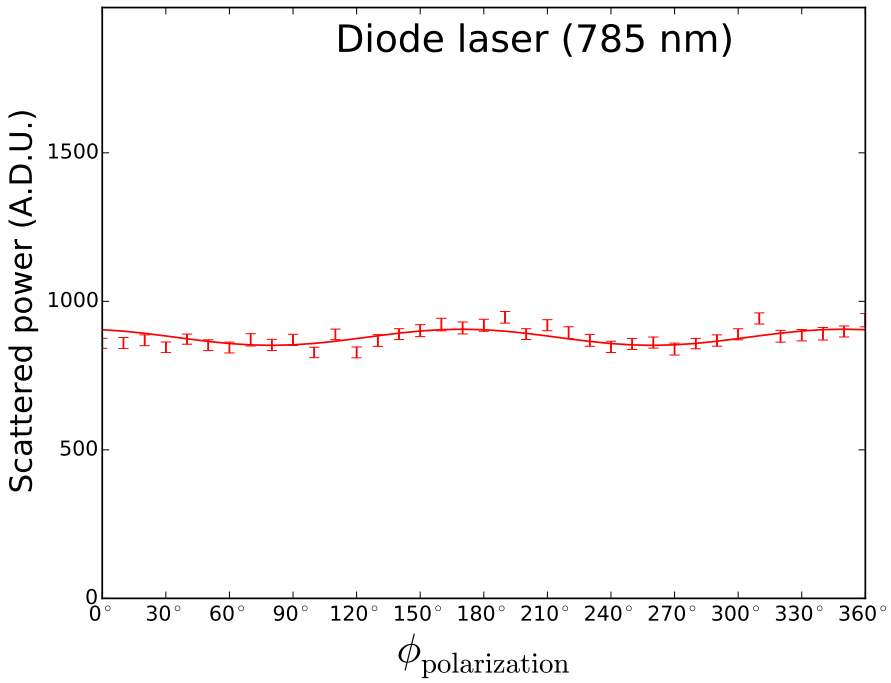

(b)

Figure B.2: Average scattered power as a function of polarisation angle for particle 2 in the first measurement, see Fig. 6.5, **a**) shows a measurement with a Helium-Neon laser and **b**) shows a measurement with a 785 nm diode laser.

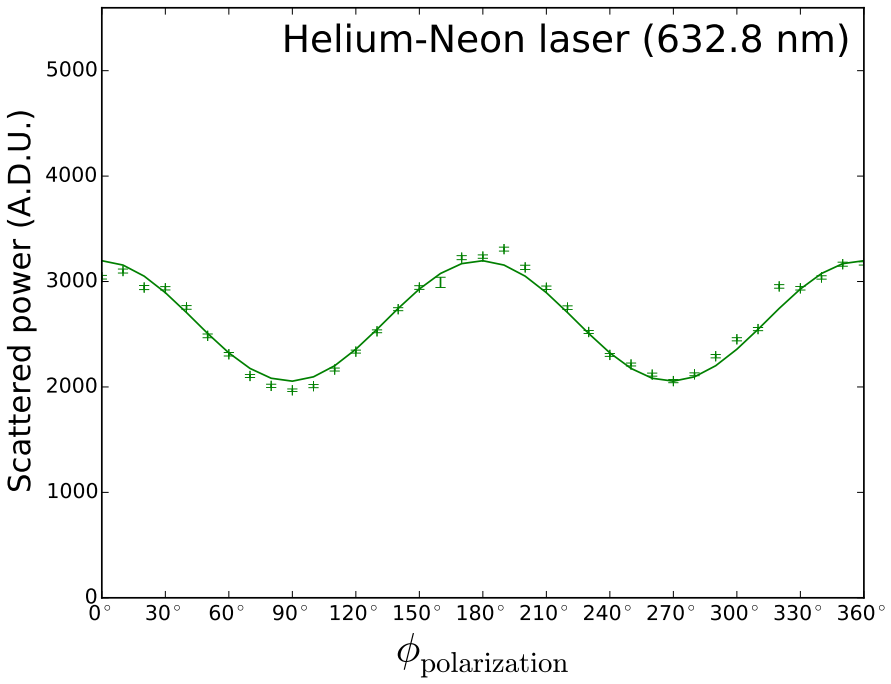

(a)

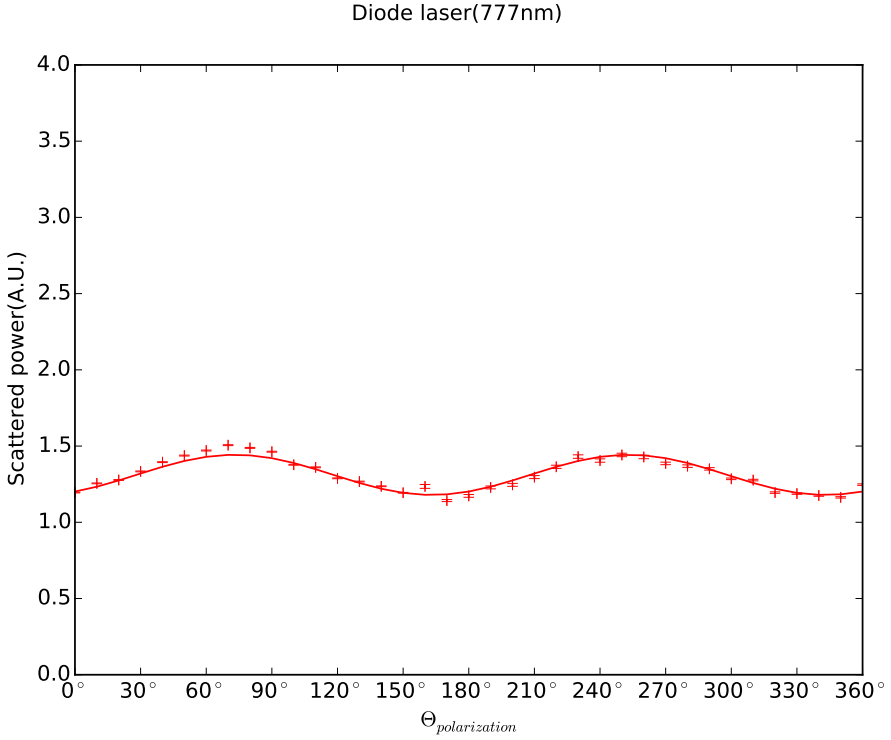

(b)

Figure B.3: Average scattered power as a function of polarisation angle for particle 3 in the first measurement, see Fig. 6.5, **a**) shows a measurement with a Helium-Neon laser and **b**) shows a measurement with a 785 nm diode laser.

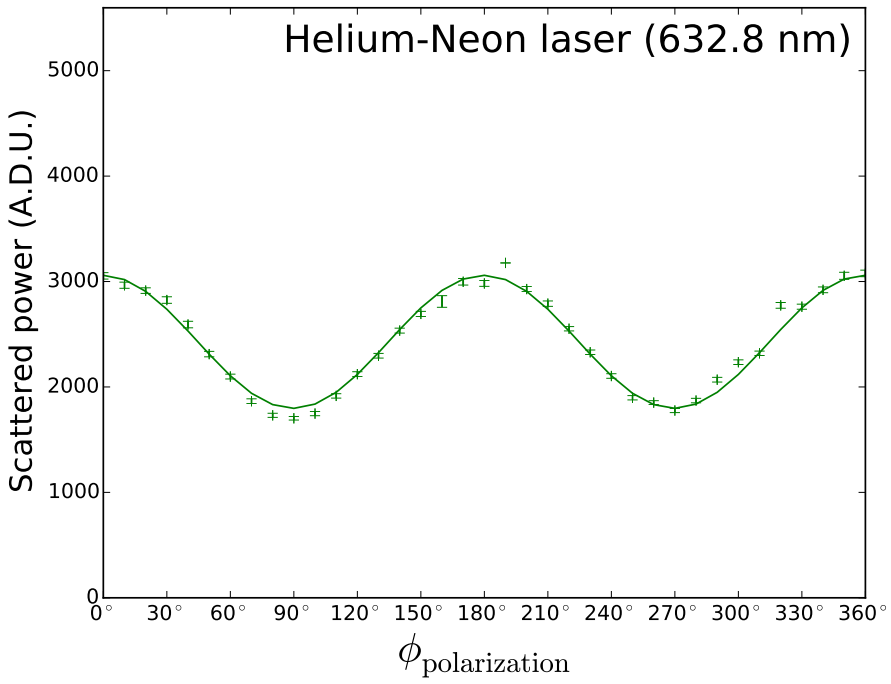

(a)

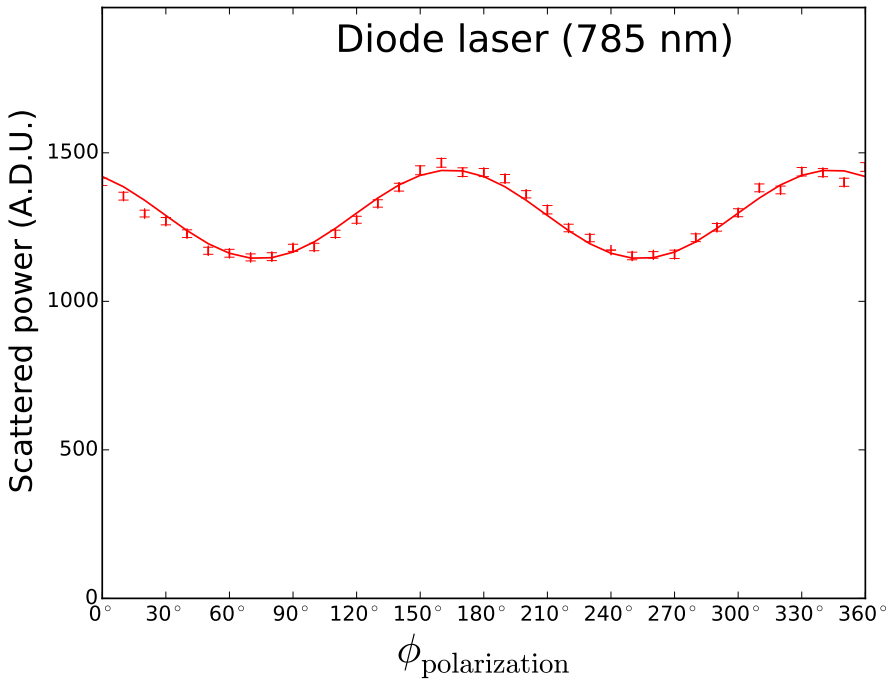

(b)

Figure B.4: Average scattered power as a function of polarisation angle for particle 5 in the first measurement, see Fig. 6.5, **a**) shows a measurement with a Helium-Neon laser and **b**) shows a measurement with a 785 nm diode laser.

9 Acknowledgements

First I would like to thank my supervisor Dries van Oosten, for his advice and council during my research project and the willingness to even look into my thesis draft during his holiday. I would like to thank Marcel Scholten, who acted as a daily supervisor throughout the year, this thesis would have been clearly worse without his constructive criticism, as well as the discussions about sports and politics. I would like to thank Javier Hernandez-Rueda, who helped to supervise me for the last couple of months of my project and helped me to do the measurements using the diode lasers, which would not have been possible in this time-frame without his assistance. I would like to thank my bachelor student Sylvianne Roscam-Abbing, she helped me do the experiments during the second half of my year and made the lab days much more lively. I would like to thank James Findley de Regt, who got me started with the electrospray setup and the trap, for being able to discuss with someone who has worked on a similar project and finally for organising great pub crawls. This project would not have been possible without the technical staff: Dante Killian and Frits Ditewig, who helped me with the electronic circuits, I would have been much more likely to electrocute myself without their assistance. Paul Jurrius, for constructing most of my setup, both of my left hands are very grateful, his quality coffee machine was also instrumental in writing my thesis. I would like to thank Cees de Kok, our laser technician, for putting up with me barging into his room all the time when I needed new stuff. I would like to thank Gordian Zomers, for helping me with the coding, especially when the software for the Grasshopper 3 camera refused to work, and Gordian helped me work around the problems. I would like to thank de rest of the section for the pleasant work environment, good advice and good borrels.

References

[1] H. Zhang *et al.*, *Single-shot femtosecond laser ablation on the nanoscale*, Ph.D. thesis, Utrecht University (2013)

[2] J. Clarijs, *Femtosecond laser nano-ablation of glass surfaces and their self-scattering effects*, Master's thesis, Utrecht University (2016)

[3] M. Scholten, *Experiments on ablation of dielectrics on gold, and water*, Master's thesis, Utrecht University (2016)

[4] G. Zomer, *Self-scattering of gold nano-particles under femtosecond laser ablation conditions*, Master's thesis, Utrecht University (2016)

[5] B. C. Stuart, M. D. Feit, S. Herman, A. M. Rubenchik, B. W. Shore, and M. D. Perry, *Nanosecond-to-femtosecond laser-induced breakdown in dielectrics*, Phys. Rev. B **vol. 53**, pp. 1749–1761 (1996)

[6] B. N. Chichkov, C. Momma, S. Nolte, F. von Alvensleben, and A. Tünnermann, *Femtosecond, picosecond and nanosecond laser ablation of solids*, Applied Physics A **vol. 63**, no. 2, pp. 109–115 (1996)

[7] L. Shah, A. Y. Arai, S. M. Eaton, and P. R. Herman, *Waveguide writing in fused silica with a femtosecond fiber laser at 522 nm and 1 mhz repetition rate*, Opt. Express **vol. 13**, no. 6, pp. 1999–2006 (2005)

[8] M. Feuerhake, J.-H. Klein-Wiele, G. Marowsky, and P. Simon, *Dynamic ablation studies of sub-micron gratings on metals with sub-picosecond time resolution*, Applied Physics A **vol. 67**, no. 5, pp. 603–606 (1998)

[9] R. Hibst and U. Keller, *Experimental studies of the application of the er: Yag laser on dental hard substances: I. measurement of the ablation rate*, Lasers in Surgery and Medicine **vol. 9**, no. 4, pp. 338–344 (1989)

[10] J. Fischer, J. Dams, M. Götz, E. Kerker, F. Loesel, C. Messer, M. Niemz, N. Suhm, and J. Bille, *Plasma-mediated ablation of brain tissue with picosecond laser pulses*, Applied Physics B **vol. 58**, no. 6, pp. 493–499 (1994)

[11] A. Sugar, *Ultrafast (femtosecond) laser refractive surgery*, Current opinion in ophthalmology **vol. 13**, no. 4, pp. 246–249 (2002)

[12] V. Y. Banine, K. Koshelev, and G. Swinkels, *Physical processes in euv sources for microlithography*, Journal of Physics D: Applied Physics **vol. 44**, no. 25, p. 253001 (2011)

[13] D. L. Matthews, E. Campbell, N. Ceglio, G. Hermes, R. Kauffman, L. Koppel, R. Lee, K. Manes, V. Rupert, V. Slivinsky, *et al.*, *Characterization of laser-produced plasma x-ray sources for use in x-ray radiography*, Journal of applied physics **vol. 54**, no. 8, pp. 4260–4268 (1983)

[14] P. Balling and J. Schou, *Femtosecond-laser ablation dynamics of dielectrics: basics and applications for thin films*, Reports on Progress in Physics **vol. 76**, no. 3, p. 036502 (2013)

[15] H. Zeng, X.-W. Du, S. C. Singh, S. A. Kulinich, S. Yang, J. He, and W. Cai, *Nanomaterials via laser ablation/irradiation in liquid: a review*, Advanced Functional Materials **vol. 22**, no. 7, pp. 1333–1353 (2012)

[16] R. Brown, *A brief account of microscopical observations made in the months of june, july and august, 1827, on the particles contained in the pollen of plants; and on the general existence of active molecules in organic and inorganic bodies.*, Philos Mag **vol. 4**, pp. 161–173 (1828)

[17] A. Einstein, *ber die von der molekularkinetischen theorie der wrme geforderte bewegung von in ruhenden flssigkeiten suspendierten teilchen*, Annalen der Physik **vol. 322**, no. 8, pp. 549–560 (1905)

[18] J. Zeleny, *Instability of electrified liquid surfaces*, Physical review **vol. 10**, no. 1, p. 1 (1917)

[19] G. Taylor, *Disintegration of water drops in an electric field*, *Proceedings of the Royal Society of London A: Mathematical, Physical and Engineering Sciences*, The Royal Society, vol. 280, pp. 383–397 (1964)

[20] Q. Xue, F. Foret, Y. M. Dunayevskiy, P. M. Zavracky, N. E. McGruer, and B. L. Karger, *Multichannel microchip electrospray mass spectrometry*, Analytical Chemistry **vol. 69**, no. 3, pp. 426–430 (1997)

[21] V. N. Morozov and T. Y. Morozova, *Electrospray deposition as a method to fabricate functionally active protein films*, Analytical chemistry **vol. 71**, no. 7, pp. 1415–1420 (1999)

[22] A. Jaworek, *Electrospray droplet sources for thin film deposition*, Journal of Materials Science **vol. 42**, no. 1, pp. 266–297 (2007)

[23] G. P. Sutton and O. Biblarz, *Rocket propulsion elements*, John Wiley & Sons (2010)

[24] W. Paul and H. Steinwedel, *Ein neues massenspektrometer ohne magnetfeld*, Zeitschrift für Naturforschung A **vol. 8**, no. 7, pp. 448–450

[25] W. Paul, *Electromagnetic traps for charged and neutral particles (nobel lecture)*, Angewandte Chemie International Edition in English **vol. 29**, no. 7, pp. 739–748 (1990)

[26] R. E. March, *An introduction to quadrupole ion trap mass spectrometry*, Journal of mass spectrometry **vol. 32**, no. 4, pp. 351–369 (1997)

[27] J. C. Schwartz, M. W. Senko, and J. E. Syka, *A two-dimensional quadrupole ion trap mass spectrometer*, Journal of the American Society for Mass Spectrometry **vol. 13**, no. 6, pp. 659–669 (2002)

[28] G. Mie, *Beiträge zur optik trüber medien, speziell kolloidaler metallösungen*, Annalen der physik **vol. 330**, no. 3, pp. 377–445 (1908)

[29] J. S. Maier, S. A. Walker, S. Fantini, M. A. Franceschini, and E. Gratton, *Possible correlation between blood glucose concentration and the reduced scattering coefficient of tissues in the near infrared*, Optics letters **vol. 19**, no. 24, pp. 2062–2064 (1994)

[30] Q. Fu and W. Sun, *Mie theory for light scattering by a spherical particle in an absorbing medium*, Applied Optics **vol. 40**, no. 9, pp. 1354–1361 (2001)

[31] S. Earnshaw, {*On the nature of the molecular forces which regulate the constitution of the luminiferous ether*}, Trans. Camb. Phil. Soc **vol. 7**, pp. 97–112 (1842)

[32] L. S. Brown and G. Gabrielse, *Geonium theory: Physics of a single electron or ion in a penning trap*, Reviews of Modern Physics **vol. 58**, no. 1, p. 233 (1986)

[33] D. Moehs, D. Church, and R. Phaneuf, *Kingdon trap apparatus and technique for precise measurement of the lifetimes of metastable levels of ions*, Review of scientific instruments **vol. 69**, no. 5, pp. 1991–1995 (1998)

[34] M. Scigelova and A. Makarov, *Orbitrap mass analyzer–overview and applications in proteomics*, Proteomics **vol. 6**, no. S2, pp. 16–21 (2006)

[35] J. W. Hager, *A new linear ion trap mass spectrometer*, Rapid Communications in Mass Spectrometry **vol. 16**, no. 6, pp. 512–526 (2002)

[36] R. E. March and J. F. Todd, *Practical aspects of ion trap mass spectrometry: Theory and Instrumentation*, vol. 3, CRC press (1995)

[37] D. Denison, *Operating parameters of a quadrupole in a grounded cylindrical housing*, Journal of Vacuum Science & Technology **vol. 8**, no. 1, pp. 266–269 (1971)

[38] J. R. Gibson and S. Taylor, *Numerical investigation of the effect of electrode size on the behaviour of quadrupole mass filters*, Rapid Communications in Mass Spectrometry **vol. 15**, no. 20, pp. 1960–1964 (2001)

[39] E. Cunningham, *On the velocity of steady fall of spherical particles through fluid medium*, Proceedings of the Royal Society of London. Series A, Containing Papers of a Mathematical and Physical Character **vol. 83**, no. 563, pp. 357–365 (1910)

[40] É. Mathieu, *Mémoire sur le mouvement vibratoire d'une membrane de forme elliptique.*, Journal de mathématiques pures et appliquées **vol. 13**, pp. 137–203 (1868)

[41] T. Hasegawa and K. Uehara, *Dynamics of a single particle in a paul trap in the presence of the damping force*, Applied Physics B **vol. 61**, no. 2, pp. 159–163 (1995)

[42] P. F. Herskind, *Cavity quantum electrodynamics with ion coulomb crystals* (2008)

[43] J. F. De La Mora, *On the outcome of the coulombic fission of a charged isolated drop*, Journal of colloid and interface science **vol. 178**, no. 1, pp. 209–218 (1996)

[44] L. Rayleigh, *On the equilibrium of liquid conducting masses charged with electricity*, The London, Edinburgh, and Dublin Philosophical Magazine and Journal of Science **vol. 14**, no. 87, pp. 184–186 (1882)

[45] http://nanocomposix.eu

[46] D. Kosters, *Isolation of single gold nanoparticles* (2014)

[47] J. Ftouni, M. Penhoat, J.-S. Girardon, A. Addad, E. Payen, and C. Rolando, *Immobilization of gold nanoparticles on fused silica capillary surface for the development of catalytic microreactors*, Chemical engineering journal **vol. 227**, pp. 103–110 (2013)

[48] C. F. Bohren and D. R. Huffman, *Absorption and scattering of light by small particles*, John Wiley & Sons (2008)

[49] J. Leinonen, *Python code for calculating mie scattering from single- and dual-layered spheres. available at http://code.google.com/p/pymiecoated/.*